DNA scaffolds enable efficient and tunable functionalization of biomaterials for immune cell modulation

Xiao Huang [1,2], Jasper Z. Williams [2,3], Ryan Chang[1], Zhongbo Li[1], Cassandra E. Burnett[4], Rogelio Hernandez-Lopez[2,3], Initha Setiady[1], Eric Gai[1], David M. Patterson[5], Wei Yu[2,3], Kole T. Roybal[2,4], Wendell A. Lim[2,3 ✉] and Tejal A. Desai [1,2 ✉]

Biomaterials can improve the safety and presentation of therapeutic agents for effective immunotherapy, and a high level of control over surface functionalization is essential for immune cell modulation. Here, we developed biocompatible immune cell-engaging particles (ICEp) that use synthetic short DNA as scaffolds for efficient and tunable protein loading. To improve the safety of chimeric antigen receptor (CAR) T cell therapies, micrometre-sized ICEp were injected intratumorally to present a priming signal for systemically administered AND-gate CAR-T cells. Locally retained ICEp presenting a high density of priming antigens activated CAR T cells, driving local tumour clearance while sparing uninjected tumours in immunodeficient mice. The ratiometric control of costimulatory ligands (anti-CD3 and anti-CD28 antibodies) and the surface presentation of a cytokine (IL-2) on ICEp were shown to substantially impact human primary T cell activation phenotypes. This modular and versatile biomaterial functionalization platform can provide new opportunities for immunotherapies.

Immune cell therapies have shown great potential for cancer treatment, but still face major challenges of efficacy and safety for therapeutic applications[1–3], for example, chimeric antigen receptor (CAR) T cell treatment[4] for a broad range of patients and solid tumours[5–9]. Immunomodulatory signals, including costimulatory ligands[10], cytokines[11–13] and checkpoint inhibitors[14], have been used extensively to boost immune cell activity and modulate tumour environment for improved efficacy[1,3]. Synthetic biocompatible materials have been employed as carriers for these biomolecules to facilitate specific localization and prolonged stability in vivo, for the modulation of natural or engineered immune cell activities[15–19].

To increase tumour-targeting specificity and avoid 'on-target, off-tumour' toxicity in bystander healthy tissues, CAR T cells have been engineered with combinatorial antigen AND-gate activation control that requires sensing two antigens on a target cell, a priming antigen to activate CAR expression and a second antigen to initiate target killing[20,21]. The clinical application of this approach, however, requires knowledge about factors that control T-cell activity, such as the tumour-associated antigen density of the AND-gate priming or CAR-targeting antigens[2]. An understanding of the density dependence of antigen-modulated T-cell activation is important for therapeutic optimization. Biomaterials presenting the priming signal (natural or synthetic antigen) at a desired density for localized activation of such engineered T cells would mitigate the safety concerns of the dual-antigen design[2,21] for translational use. Additionally, synthetic materials with multivalent and multimodal biofunctionalization could advance the needs of cell modulation in immunotherapies[22–26]. Antibody–antigen binding on surfaces requires a certain spatial threshold based on the spatial tolerance of

the specific antibody[27], and therefore a high and controllable density of surface biomolecules could allow for precise control of ligand binding and cell modulation.

Currently, there is an unmet need for robust and biocompatible conjugation strategies to functionalize the surface of biodegradable materials with biomolecules (particularly proteins/antibodies) at high densities and to present multiple moieties at precisely controlled ratios[28–30]. Polyethylene glycol (PEG) is commonly used as a linker or scaffold for bioconjugation[29], but this method is limited by inefficient presentation of functional groups due to the flexibility of PEG[31]. The surface functionalization of multiple biomolecules and their ratiometric control mostly rely on streptavidin-based chemistry[32] or orthogonal conjugation strategies[33], which can be substantially affected by the chemical properties of the specific cargos. Oligonucleotides have been used as building blocks for origami structures with a controlled display of proteins[34,35] and as surface scaffolds on metallic particles for short interfering RNA delivery[31,36,37], but have yet to be fully utilized for modular and multimodal protein assembly on biodegradable materials[38]. Synthetic short oligonucleotides—natural polymers with a controllable sequence and unique assembly through Watson–Crick base pairing[35,39]—would be ideal mediators for controlled surface functionalization of biomolecules.

Here, we developed short synthetic DNA scaffolds for the functionalization of biomolecules on the surface of biodegradable particles to extend the immunomodulatory potential (Fig. 1a). For our demonstration platform, we fabricated micrometre-sized immune cell-engaging particles (ICEp) using a biocompatible poly(lactic-co-glycolic acid) (PLGA) polymer[40]. DNA strands were immobilized on the surface of polymeric particles through

[1]Department of Bioengineering and Therapeutic Sciences, University of California, San Francisco, San Francisco, CA, USA. [2]Cell Design Institute and Center for Synthetic Immunology, University of California, San Francisco, San Francisco, CA, USA. [3]Department of Cellular and Molecular Pharmacology, University of California, San Francisco, San Francisco, CA, USA. [4]Department of Microbiology and Immunology, University of California, San Francisco, San Francisco, CA, USA. [5]Department of Pharmaceutical Chemistry, University of California, San Francisco, San Francisco, CA, USA. ✉e-mail: wendell.lim@ucsf.edu; tejal.desai@ucsf.edu

an emulsion protocol to create an adaptable scaffold for loading bioactive molecules (Supplementary Fig. 1a). Polymer–DNA amphiphilic molecules were synthesized with optimizations, including the choice of the polymer, DNA length, solvent and reaction conditions, to form stable PLGA particles with dense DNA scaffolds (Supplementary Fig. 1b–f). The direct incorporation of the reaction mixtures with increasing yield of polymer–DNA conjugate (from varying ratios of thiol-modified DNA to PLGA10k-PEG5k-maleimide) into the emulsion protocol yielded a continuous increase of surface payload-attachable DNA scaffold density (Fig. 1b,c and Supplementary Fig. 1d). Strikingly, the highest average surface loading density on particles (~5 million DNA duplexes per particle, Supplementary Fig. 1g–i) was roughly analogous to the theoretical limit (at ~4 million by footprint calculation, based on ~2 nm diameter of the DNA duplex) of a spherical particle with a diameter of 2 μm. In particular, this hybridization-guided loading was about 27-fold more efficient than loading from a traditional method[41], in which surface-exposed maleimide groups, after particle fabrication using an equal amount of PLGA10k-PEG5k-maleimide, were reacted with thiol-modified DNA molecules (Fig. 1b,c). This hybridization-guided assembly protocol is biocompatible, convenient and rapid, such that incubation at room temperature for 2 min achieved ~87% of the maximum loading (Fig. 1d and Supplementary Fig. 1j-l).

Furthermore, using unique DNA nucleotide sequences enables independent control of loading multiple cargos on the same material surface (Fig. 1e). Polymer–DNA conjugates with three distinct DNA sequences (namely R, G and B strands, Supplementary Fig. 2a) were incorporated into the particle emulsion with reaction mixtures at different ratios (3:1:1, 1:1:1 and 1:1:3). After the strands were surface hybridized with a mixture of their respective dye-labelled complementary strands (Fig. 1e), we observed that the ratios of hybridized DNA scaffolds of different sequences on PLGA microparticles were consistent with the polymer–DNA conjugate input (Fig. 1f–h). The ratio of hybridized duplexes is determined by the ratio of surface DNA scaffolds of specific sequences and is rarely affected by the ratio of complementary strands (Supplementary Fig. 2b). In contrast, ratiometric control of such dye-labelled DNA strands on particles using a canonical streptavidin-based method (Supplementary Fig. 2c) was not successful (Supplementary Fig. 2d), which may be affected by the chemical properties of the cargo.

The biocompatibility and biodegradability of the core polymer make this strategy well suited for in vivo applications, and the degradation profile can be easily tuned through the choice of polymer[40]. For example, DNA-scaffolded microparticles can be fabricated using the more stable polymer poly(lactic acid) (PLA) and achieve ratiometric control of DNA scaffolds (Supplementary Fig. 2e–j).

To accommodate diverse applications, from intracellular payload delivery to extracellular signal transduction, DNA-scaffolded particles can be synthesized at various sizes and loaded with biomolecules in their core. Particle size can be controlled by tuning key emulsion parameters (Supplementary Fig. 2k,l). Additionally, the core of these particles can be loaded with biomolecules, including oligonucleotides and peptides, through a double-emulsion protocol (Supplementary Fig. 2m–o).

Highly efficient loading of multiple proteins with ratiometric control

Biomolecules can be loaded onto the surface of DNA-scaffolded particles using one of two strategies: (1) through a surface step-by-step conjugation via a bifunctional linker; and (2) through direct hybridization of complementary DNA–biomolecule conjugates to the scaffold (Fig. 2a). In the case of a fluorescently labelled human IgG, surface step-by-step conjugation saturated the protein loading, even with increased densities of available DNA linkers on the surface (Figs. 1c and 2b and Supplementary Fig. 3a). In contrast, the hybridization-guided assembly strategy showed an approximately threefold higher level of IgG loading than the surface-conjugation method for particles with denser DNA scaffolds ($P = 0.0002$), and the increase in IgG loading corresponded to the increase in scaffold density (Fig. 2b). The highest level of IgG loading achieved (at ~0.6 million per particle) was again comparable to the theoretical footprint limit of a spherical particle at 2 μm in diameter (~0.64 million per particle, based on ~5-nm diameter of IgG) (Fig. 2b). To generate DNA–antibody conjugates with minimal impact on antibody activity, a 'TCEP' strategy[42] was chosen, whereby the antibody hinge region was selectively reduced to expose the thiol group to conjugate with a complementary DNA strand. Using this conjugation strategy, anti-PD-L1 antibody, a checkpoint inhibitor, showed intact binding activity (Supplementary Fig. 3b,c), and its loading on PLGA microparticles resulted in high binding specificity for PD-L1-positive cells (Fig. 2c). In addition, increasing levels of anti-PD-L1 loading from varying densities of DNA scaffolds on particles (Fig. 2b, low, medium and high density) correlated to increasing levels of PD-L1 antigen binding (Fig. 2d–f). For DNA tethering of proteins other than antibodies, other conjugation options are available to yield products with intact activity (Supplementary Fig. 3d,e).

Using ratiometrically controlled sequences on PLGA particles (Fig. 1f,g), we co-loaded three proteins (GFP and two antibodies), each individually attached to one of the three unique complementary DNA strands, through hybridization-guided assembly (Fig. 2g). The distribution of each protein cargo correlated to the respective scaffold population (Fig. 2h,i), demonstrating the robust ratiometric control achieved using this strategy. We also tested the

Fig. 1 | Polymeric micro-/nanoparticles with surface DNA scaffolds for protein presentation allow versatile modulation of immune cell therapies. a, Schematic of biodegradable polymeric particles presenting therapeutic proteins via surface DNA scaffolds with high density and ratiometric control, and their potential use as ICEp for tumour microenvironment modulation and localized activation of natural or engineered immune cells. N, normal tissue; C, cancer cell; T; T cell;, P, ICEp. **b**, Schematic showing the construction of high and controlled densities of DNA scaffolds on polymeric particles through a self-display of amphiphilic polymer–DNA molecules during the emulsion process, compared to the traditional surface-conjugation method after particle fabrication. **c**, Fluorescence-based analysis of hybridized, dye-labelled DNA duplexes on PLGA particles made from DNA–polymer conjugates of different coupling efficiencies versus dye-labelled DNA that was surface conjugated to exposed functional groups on particles. Data are mean ± s.d. ($n = 6$ independent samples from three independent experiments) and P values were determined by one-way ANOVA and Tukey's tests. **d**, Photographs of PLGA microparticles in Eppendorf tubes after adding Q670-labelled complementary DNA to a matched or unmatched sequence for 2 min at room temperature. **e**, Schematic displaying the control of DNA scaffolds with distinct sequences at intended ratios, which is confirmed by a corresponding dye-labelled complementary DNA (compDNA) hybridization assay. **f**, Representative confocal microscopy images of PLGA microparticles with DNA scaffolds of different sequence compositions after hybridization with corresponding dye-labelled compDNA. The merged images of particles agreed with the theoretically integrated colour at different input ratios. Scale bar, 5 μm. **g**, Fluorescence-based analysis of DNA duplexes of different sequences on particles shown in **f**. Data are mean ± s.d. ($n = 5$ independent samples from two independent experiments) and P values were determined by one-way ANOVA and Tukey's tests. **h**, Correlation between hybridized duplexes of specific sequences on the surface and their corresponding DNA–polymer conjugate inputs shown in **g**. Data are mean ± s.d. ($n = 5$ independent samples from two independent experiments) and the linear regression was created from individual replicates ($R^2 = 0.8501$) and the mean of each condition ($R^2 = 0.9516$).

ratiometric control of biotinylated proteins (GFP and two antibodies tagged with different fluorescent dyes) on streptavidin-coated particles, but this streptavidin-based strategy showed limited control (Supplementary Fig. 3f).

Compatibility of this platform for in vivo applications

To enable in vivo use, we explored the stability of the DNA scaffolds on PLGA microparticles in the presence of a large excess of DNase (Fig. 3a). We observed an almost complete (~87%) degradation of

DNA scaffolds after DNase treatment; however, this dropped to ~20% with moderate IgG coverage (~¼ of the highest IgG loading) (Fig. 3b). This suggests that surface-loaded proteins are able to protect DNA scaffolds through steric hindrance. In human serum, we did not observe as much DNA degradation for the non-scaffolded particles (~29%), which may be due to the comparatively lower levels of DNase in serum than used in Fig. 3a,b; however, the degree of DNA degradation similarly decreased when proteins were attached to the surface (Fig. 3c).
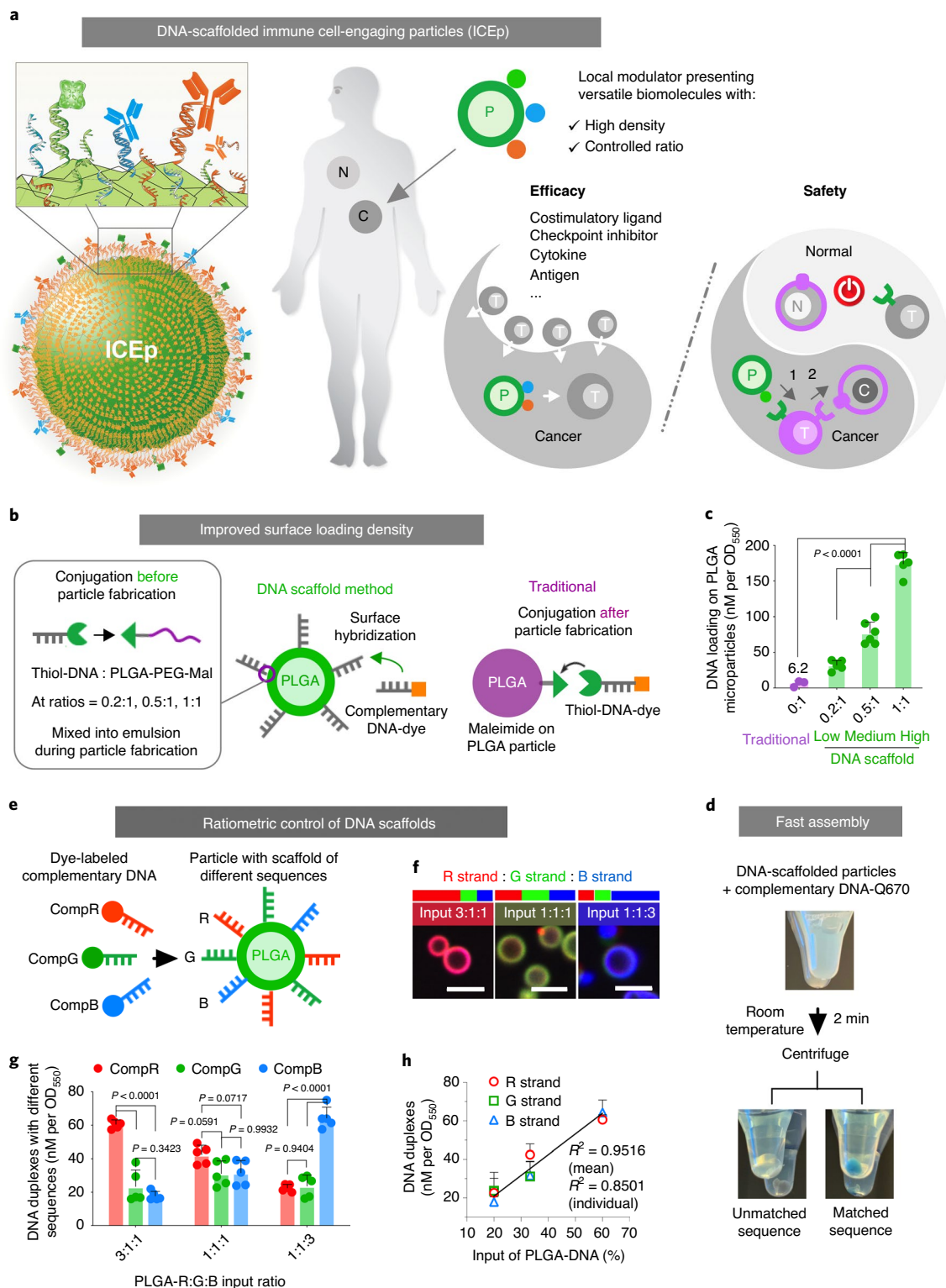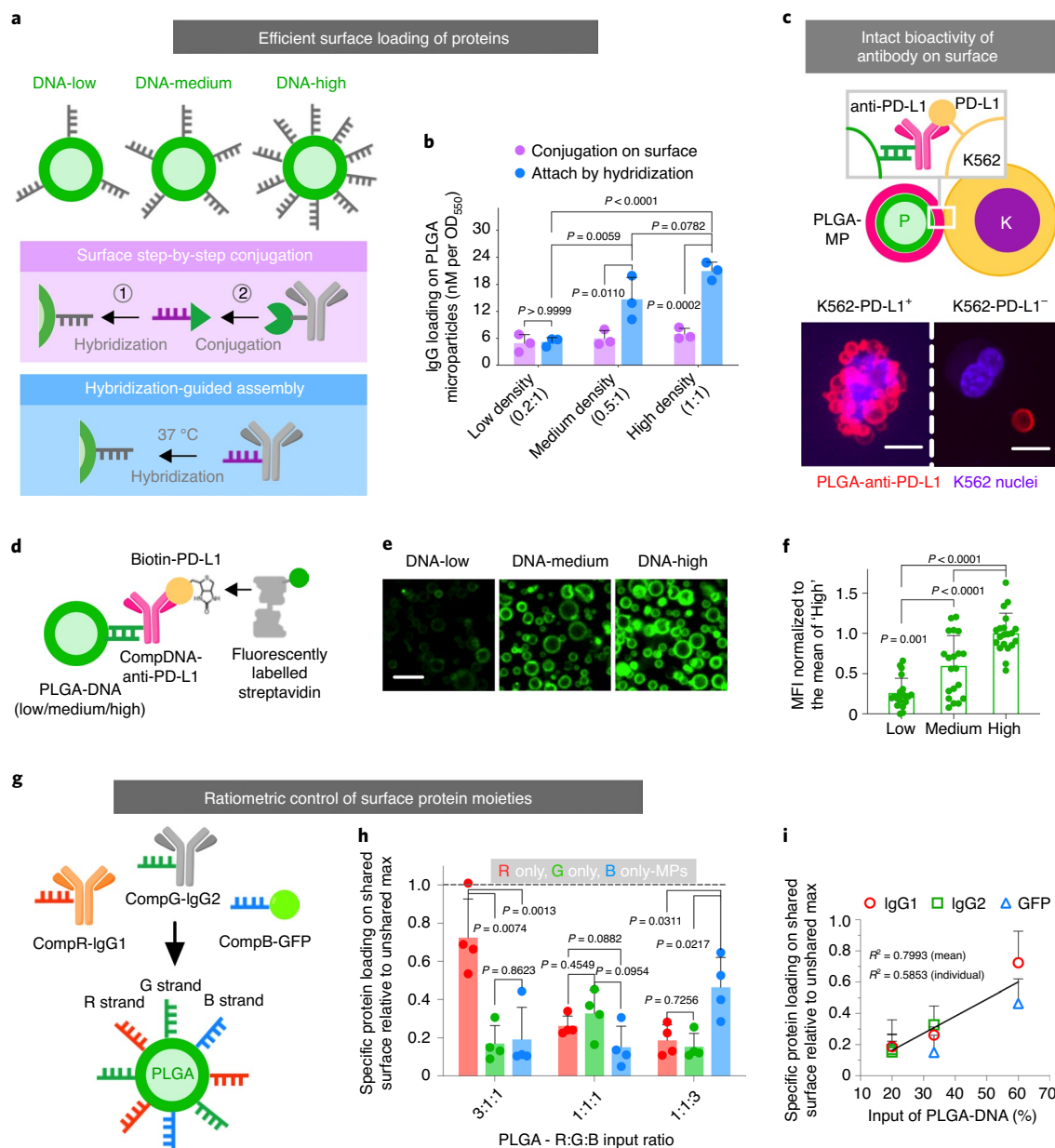
Fig. 2 | DNA scaffolds enable efficient loading of multiple therapeutic proteins on particle surfaces at precisely tunable ratios. a, Schematic of two strategies of protein loading on particles with DNA scaffolds: (i) step-by-step conjugation through a bifunctional linker, and (ii) hybridization-guided assembly of complementary DNA–protein conjugates. **b**, Quantification of the FITC-labelled IgG loading density by the two strategies depicted in **a**. Data are mean ± s.d. (n = 3 independent experiments) and P values were determined by one-way ANOVA and Tukey's tests. **c**, Schematic of a PLGA microparticle (MP) loaded with an anti-PD-L1 antibody binding to PD-L1-expressing K562 cells. Representative confocal microscopy images of co-incubated anti-PD-L1-tethered particles and PD-L1$^{+/-}$ K562 cells (n = 3 biologically independent samples per group). Scale bar, 10 μm. **d**, Schematic of a method that tests antigen-binding activity of surface-loaded antibodies. Biotinylated PD-L1 was used to bind active anti-PD-L1 on the particle surfaces, followed by the binding of fluorescently labelled streptavidin for detection. **e**, Representative confocal microscope images of PLGA microparticles with different densities of DNA scaffolds that have been loaded with anti-PD-L1 antibodies followed by the assay described in **d** (n = 20 images from four independent experiments). Scale bar, 5 μm. **f**, Quantification of the MFI of particles in images shown in **e**. Data are mean ± s.d. (n = 20 images from four independent experiments) and P values were determined by one-way ANOVA and Tukey's tests. **g**, Schematic showing how PLGA particles with DNA scaffolds composed of distinct sequences enable the loading of specific ratios of therapeutic proteins. **h**, Fluorescence-based analysis of the loading densities of three different proteins on the same surface guided by DNA scaffold compositions, relative to their individual, unshared maximums (max). Data are mean ± s.d. (n = 4 independent samples from three independent experiments) and P values were determined by one-way ANOVA and Tukey's tests. **i**, Correlation between the specific protein loading on the surface and their corresponding DNA–polymer conjugate input during particle fabrication shown in **e**. Data are mean ± s.d. (n = 3 independent experiments), and the linear regression was created from individual replicates ($R^2 = 0.5853$) and the mean of each condition ($R^2 = 0.7993$).

We evaluated the feasibility of using local particle delivery to send spatially defined signals to therapeutic cells in vivo. We labelled DNA scaffolds on PLGA microparticles with infrared dye Quasar705 (Q705), and we monitored the distribution and half-life of their surface coating through in vivo imaging system (IVIS) near-infrared fluorescence after injecting particles intratumorally
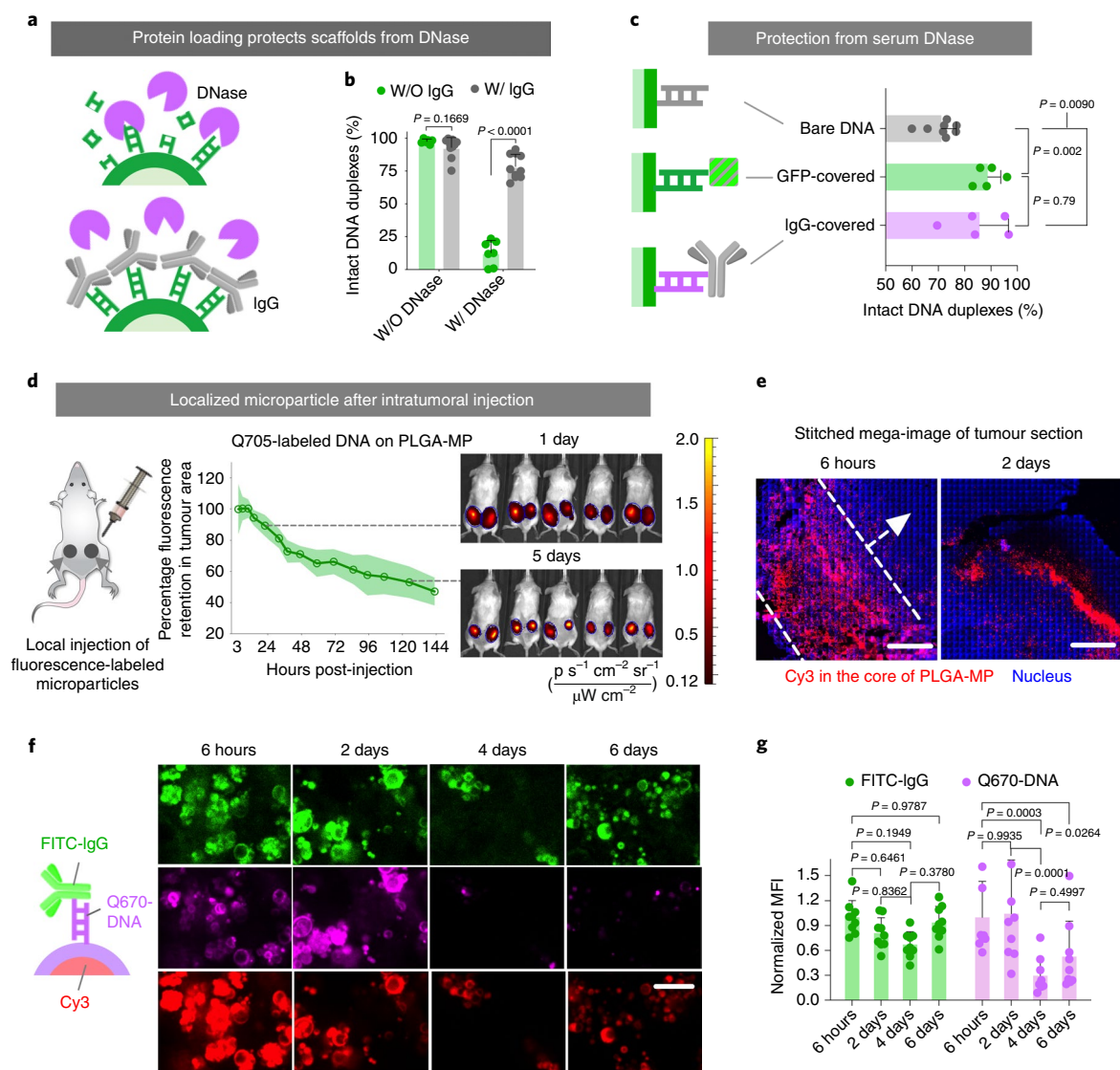
Fig. 3 | Compatibility of DNA-scaffolded PLGA particles for in vivo applications. a, Schematic showing that DNA scaffolds on the surface can be protected from DNase degradation by protein attachment. **b**, Fluorescence-based analysis of intact DNA duplexes on PLGA microparticles after co-incubating with a large excess of DNase for 20 min. W/O, without; W/, with. Data are mean ± s.d. ($n = 3$ independent experiments) and P values were determined by two-tailed paired t-test. **c**, Fluorescence-based analysis of intact DNA duplexes with different protein attachments on PLGA microparticles after incubation in human serum for 1 h. Data are mean ± s.d. ($n = 8$ independent samples for 'Bare DNA' and 5 independent samples for 'GFP-covered' and 'IgG-covered', from two independent experiments) and P values were determined by one-way ANOVA and Tukey's tests. **d**, IVIS fluorescence imaging of NSG mice with subcutaneous K562 tumours that were injected with microparticles loaded with Q705-labelled compDNA and human IgG over 6 days (herein, day 1 and 5), and quantification of signal intensity at the tumour area (right tumour with ICEp-PLGA) for the full set of IVIS images acquired over 6 days relative to 3 h. Lines connect the means of relative signal intensity from $n = 5$ mice, and the shaded area denotes the error band (±s.d.). **e**, Representative stitched confocal microscope images of subcutaneous K562 tumour sections from NSG mice that were injected with Cy3 dye conjugated (in the core) PLGA microparticles (with compDNA and human IgG on the surfaces) for 6 h and 2 days ($n = 3$ mice). Scale bar, 1 mm. **f**, Representative confocal microscope images of subcutaneous K562 tumour sections from NSG mice that were injected with PLGA microparticles with Cy3 dye conjugated in the core, Q670-labelled compDNA and FITC-IgG on the surfaces at different time points, ranging from 6 h to 6 days ($n = 15$ images from three mice at each time point). Scale bar, 20 μm. **g**, Quantification of the mean fluorescence intensity (MFI) of Q670-compDNA and FITC-IgG on microparticles in the tumour section images shown in **f**. Data are mean ± s.d. ($n = 9$ images for 6 h, 2 days and 4 days, and 6 images for 6 days, from three mice at each time point) and P values were determined by one-way ANOVA and Tukey's tests.

in NSG mice with subcutaneous K562 xenograft tumours (Fig. 3d). Microparticles with diameters of ~2 μm were retained locally within the tumour (Fig. 3d and Supplementary Fig. 4a) for more than a week, with a gradient distribution around the injection site (Fig. 3e) and minimal distribution to other organs (Supplementary Fig. 4b,c). Fluorescence quantification of IVIS images and tumour sections showed stable surface loading on particles with a half-life

of ~2–4 days (Fig. 3d,f,g), while free dye signal without particle carriers diminished rapidly after 6 hours (Supplementary Fig. 4d,e). These results demonstrate that injections of DNA-scaffolded microparticles can be used to send localized, sustained signals to therapeutic cells in vivo.

We then investigated the safety of intravenous injection of DNA-scaffolded particles (carrying ~20 μg isotype IgG) in BALB/c

mice by serum cytokine/chemokine quantification (mouse cytokine/chemokine 31-plex) and clinical chemistry analysis of blood collected 2 days later. Treatments with PLGA nanoparticles (~250 nm diameter) and microparticles (~1.5 µm diameter) tethered with DNA scaffolds and mouse isotype IgG both showed similar levels of blood cytokines compared to the PBS treatment control (Supplementary Fig. 4f). The blood clinical chemistry values for micro- and nanoparticles were comparable to the PBS control, all falling within the normal range as referenced from the University of Arizona animal care (Supplementary Fig. 4g).

Since macrophage uptake could be an obstacle[43] for particle-based drug delivery in vivo, we incorporated a CD47-mimic 'self'-peptide[44] onto DNA-scaffolded PLGA microparticles to reduce possible phagocytosis by macrophages (Supplementary Fig. 4h). Fluorescein-labelled PLGA microparticles with and without the surface-loaded self-peptide were co-incubated with a mouse macrophage line J774A.1 in vitro. The surface decoration of a self-peptide significantly reduced the uptake of these particles by macrophages (Supplementary Fig. 4h,i, $P = 0.0004$). This self-peptide functionalization provides a possible strategy to reduce the clearance of particles in vivo.

Design of particles to prime activation of AND-gate CAR-T cells

We tethered an orthogonal antigen (GFP) on micrometre-sized ICEp to prime AND-gate CAR-T cells engineered with antigen-recognition circuits, thus restricting CAR T cytotoxicity to tumours locally injected with microparticles (Fig. 4a). These AND-gate T cells utilize a modular synthetic Notch (synNotch) receptor with an extracellular domain to recognize a target antigen and an intracellular transcriptional activator (TF) domain to control the expression of a CAR targeting a second antigen[20]. Killing is only induced when both antigens are presented to T cells, with one activating the synNotch receptor to release the TF domain for CAR expression and the other activating CAR-mediated cytotoxicity[20]. Herein, human primary T cells were transduced with a gene encoding a constitutively expressed synNotch receptor with an extracellular anti-GFP nanobody and an intracellular Gal4DBD-VP64 synthetic TF domain, together with a TF-inducible CAR gene targeting human epithelial growth factor receptor 2 (HER2)[20] (Fig. 4a). In this system, T cells only express anti-HER2 CAR and kill

HER2-positive target cells after being primed by the anti-GFP synNotch binding of ICEp-presented GFP.

Human primary CD8^{+} T cells engineered with the synNotch receptor-CAR circuit were cocultured for 24 hours with single-antigen target cells (human melanoma cell line A375 with HER2 overexpressed) in the presence or absence of GFP[+] ICEp microparticles. SynNotch CAR-T cells showed selective expression of the early activation marker CD69 in the presence of both HER2^{+}A375 cells and GFP[+] ICEp, and the activation was similar to T cells exposed to dual-antigen target cells (human leukaemia cell line K562 with GFP and HER2 co-expressed) (Supplementary Fig. 5a). Engineered T cells also showed AND-gate killing behaviour, selectively killing HER2^{+}A375 cells in the presence of ICEp microparticles with GFP (Fig. 4b,c and Supplementary Fig. 5b–d). Importantly, we observed density-dependent activation of the synNotch receptor for cytokine release in both CD4^{+} and CD8^{+} CAR-T cells (Fig. 4d and Supplementary Fig. 5e) and target killing by CD8^{+} cells (Fig. 4e). ICEp presenting a lower density of the GFP antigen may result in inadequate expression of HER2 CAR on T cells for robust activity, explaining why initial attempts using particles functionalized by traditional surface-conjugation chemistry and with a far lower GFP density failed to activate synNotch CAR-T cell toxicity (Fig. 4e). Importantly, antigen-presenting ICEp showed notable advantages in the activation of murine immune cell lines compared to antigen-presenting K562 cells (Fig. 4f,g, $P < 0.0001$ for all three), demonstrating the usefulness of this platform for logic-gated cell modulation.

When saturated densities of GFP were loaded on ICEp of different sizes ('nano', 'medium' and 'micro', corresponding to Supplementary Fig. 2l), they activated CD8^{+} synNotch CAR-T cells and had similar efficiencies of killing to the target HER2^{+}A375 cells (Supplementary Fig. 5f). The co-incubation of target cells with synNotch CAR-T cells in the absence of ICEp showed moderate cytotoxicity (Fig. 4c and Supplementary Fig. 5b–d,f), which is probably due to the leakiness of inducible CAR expression. This phenomenon was also observed in previous reports and can be improved through further optimization of synNotch receptors.

We hypothesized that GFP-decorated PLGA microparticles could be injected intratumorally as a local activator for systemically administered anti-GFP synNotch/anti-HER2 CAR-T cells

Fig. 4 | Local activation of AND-gate CAR-T cell for tumour killing by intratumoral injection of ICEp presenting a priming antigen. a, Schematic showing the use of ICEp to present synthetic priming antigens (GFP) via intratumoral (i.t.) injection to locally prime synNotch CAR AND-gate T cells to kill tumour cells. Primary human T cells were engineered with the anti-GFP synNotch and corresponding response elements regulating anti-HER2 4-1BB CAR expression. The synNotch CAR-T cells only express the CAR after sensing ICEp-presented GFP via synNotch binding, which should reduce on-target, off-tumour toxicity to healthy organs also expressing the CAR antigen. **b**, Representative confocal fluorescence microscopy image of the co-incubation of CD8^{+} synNotch CAR-T cells, ICEp-GFP and HER2-overexpressing A375 cells after 24 h ($n = 2$ independent experiments). Scale bar, 10 µm. **c**, Target A375 cell killing test 48 h after coculture with ICEp-GFP and synNotch CAR-T cells. Data are mean ± s.d. ($n = 6$ independent experiments with four independent T-cell donors), and P values were determined by one-way ANOVA and Tukey's tests. **d**, IL-2 secretion by primary human CD4^{+} T cells after a 48-h coculture with HER2^{+}A375 target cells and ICEp with different GFP densities (for example, 1/3, ½ and full). The total amount of antigen presented to T cells by ICEp particles with 'Full' was equal to '1/3×3'. Data are mean ± s.d. ($n = 4$ biologically independent samples from two independent experiments) and P values were determined by one-way ANOVA and Tukey's tests. **e**, Killing efficacy of HER2^{+}A375 cells after a 48 h coculture with AND-gate T cells that were primed by ICEp with varying densities of GFP from DNA scaffolds, compared to traditional conjugation chemistry. Images are representative confocal fluorescence microscopic images of ICEp. Data are mean ± s.d. ($n = 16$ biological replicates from four independent experiments) and P values were determined by one-way ANOVA and Tukey's tests. **f**, Schematic of ICEp-GFP versus GFP-expressing K562 cells activating murine immune cell lines that were engineered with anti-GFP synNotch and corresponding response elements regulating BFP expression. **g**, The population of BFP[+] murine immune cells that were activated by ICEp-GFP compared to GFP-expressing K562 cells and K562 cells without GFP antigen. Data are mean ± s.d. ($n = 3$ biological replicates) and P values were determined by one-way ANOVA and Tukey's tests. **h**, Schematic of the NSG mice two-tumour model for selected clearance by ICEp-primed synNotch CAR-T cell activation, while ICEp-GFP and engineered human primary CD4^{+}/CD8^{+} T cells were administered through i.t. and intravenous (i.v.) injection, respectively. **i**, Comparison between the volumes of the ICEp-injected tumour and the contralateral tumour of mice treated with engineered synNotch CAR-T cells (left graph) or untransduced T cells (right graph). Data are mean ± s.e.m. ($n = 8$ mice, and two mice met the euthanasia criteria at day 13–15) and P values were determined by two-tailed paired t-test. **j**, Representative images of fixed staining of tumour sections from one mouse that was killed on an earlier date (day 15) that met euthanasia criteria ($n = 10$ images). Scale bar, 50 µm. **k**, Quantification of CD3^{+} T cell numbers in the stained tumour sections represented in **j**. Data are mean ± s.d. (from $n = 10$ images) and P values were determined by two-tailed paired t-test.

(Fig. 4h). NSG mice were implanted subcutaneously with the same HER2-overexpressed K562 xenograft tumours in their bilateral flanks as a model for tumour and healthy tissue, both expressing the CAR antigen. After a week, mice were intravenously administered synNotch CAR-T cells once in combination with four doses of intratumorally injected ICEp (Fig. 4h). The size of ICEp-injected ipsilateral tumours decreased over time, in contrast to the

contralateral tumours within the same mice without ICEp injection and tumours in mice injected with ICEp plus untransduced primary T cells (Fig. 4i and Supplementary Fig. 5g). We also performed fluorescence microscopy on fixed tumour samples of mice killed at an earlier time point (day 15) and observed selective T-cell enrichment in the ICEp-injected tumour (Fig. 4j,k). These results demonstrate that ICEp can provide spatially controlled signals in vivo for the

NATURE NANOTECHNOLOGY | www.nature.com/naturenanotechnology
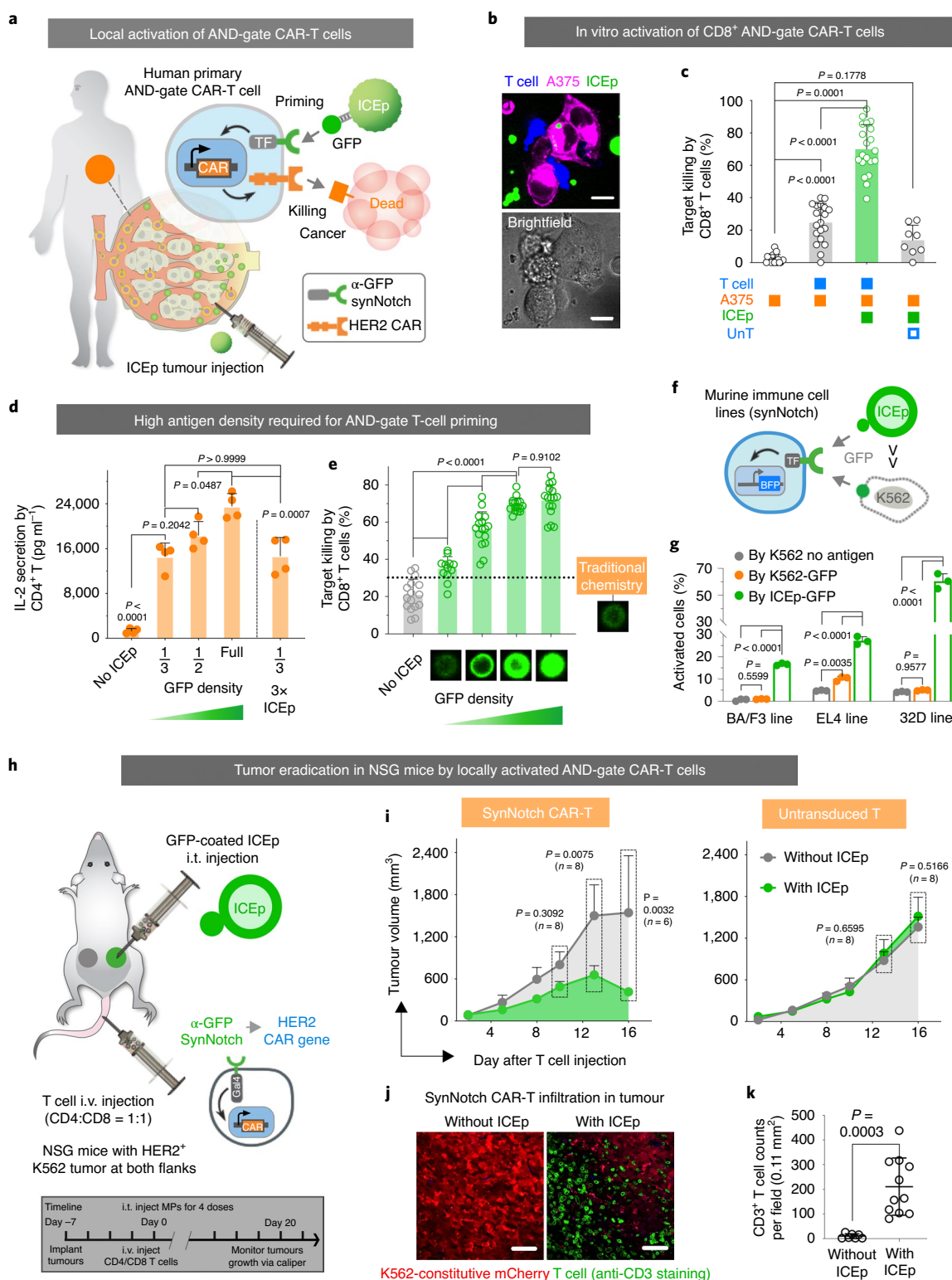
local activation of synNotch CAR-T cells and induction of tumour clearance with limited risk of cross-reaction against healthy tissues.

Design of optimized particles for natural T-cell activation

To demonstrate the versatility of this platform for immune cell modulation, we engineered T-cell costimulatory ligands anti-CD3 and anti-CD28 on biodegradable PLGA microparticles, termed anti-CD3/CD28 ICEp, to activate human primary T cells ex vivo (Fig. 5a,b and Supplementary Fig. 6a). Starting with the same particle-to-cell ratio as commercial anti-CD3/CD28 Dynabeads, T cells underwent massive expansion with a cell yield that is higher at day 8 and equivalent at day 14 to that of Dynabead-mediated activation across three independent CD4+ and CD8+ T cell donors (Fig. 5c and Supplementary Fig. 6b). To investigate the exhaustion phenotype of expanded CD4+ and CD8+ T cells at day 14, we examined cell exhaustion markers LAG-3, PD-1 and TIM-3 (Supplementary Fig. 6c). With the added benefit of not having to remove degradable ICEp (Supplementary Fig. 6a), we found that the populations of exhaustion marker-positive cells among the three donors were consistent and generally lower with ICEp, compared to those activated by Dynabeads (Fig. 5d and Supplementary Fig. 6d). We also reduced the total amount of anti-CD3 and anti-CD28 on ICEp from 'Full' to '1/5' (Supplementary Fig. 6e) and found that the impact of lowering antibody density on CD8+ T-cell expansion is donor dependent: two donors showed significantly less cell expansion (D1, $P = 0.0306$; D2, $P = 0.0457$), while three others showed significantly more expansion (D3, $P = 0.0023$; D4, $P = 0.0193$; D5, $P = 0.0457$) (Supplementary Fig. 6f).

Given the ability of this platform to precisely control the ratio of multiple surface proteins, we modulated anti-CD3 and anti-CD28 antibodies on ICEp at ratios ranging from 1:5 to 5:1 to activate human T cells and observed a linear increase of cell yield from ICEp-[1:5] to ICEp-[3:1] for both CD4+ and CD8+ cells at day 14 (Fig. 5e,f). For CD8+ T cells, the exhaustion phenotype (population of 0, 1–3 exhaustion marker expression) was significantly different between ICEp-[1:5]- and ICEp-[3:1]-mediated activation for 14 days among the three donors (Fig. 5g, $P = 0.0003$). For CD4+ T cells, only the population of non-exhausted cells was significantly different between the two ratios (Supplementary Fig. 6g, $P = 0.0068$). Additionally, the cell differentiation phenotype of T cells on day 7 after ICEp activation was explored by measuring the expression of CD45RA and CCR7 surface markers (Fig. 5h). The cell populations of each gated quadrant between

ICEp-[1:5]- and ICEp-[3:1]-mediated activation were significantly different within a donor (Fig. 5i, CD45RA+CCR7+, $P < 0.0001$; CD45RA−CCR7+, $P = 0.0016$; CD45RA−CCR7−, $P < 0.0001$; CD45RA+CCR7−, $P = 0.0044$). With a flow cytometry panel (CD45RA, CCR7, CD27, CD45RO, CD62L and CD95) analysis[45] (the same donor), we observed a dramatically different pattern of cell differentiation between ICEp-[1:5]- and ICEp-[3:1]-mediated activation and identified that the population of CD45RA+CCR7+ cells are also CD45RO+ and are, therefore, central memory cells (Supplementary Fig. 6h). Among five donors, the cell differentiation phenotype represented by the expression of CD45RA and CCR7 markers (CD45RA+CCR7+ and CD45RA−CCR7+: central memory, CD45RA−CCR7−: effector memory, CD45RA+CCR7−: terminally differentiated effector memory) showed a dramatic difference between ICEp-[1:5]- and ICEp-[3:1]-mediated activation as well (Supplementary Fig. 6i, $P < 0.0001$). Overall, we demonstrated that key immune cell properties, from cell expansion to exhaustion and differentiation phenotypes, are impacted by the ratiometric control of anti-CD3 and anti-CD28 on ICEp, thus highlighting potential new opportunities for immune cell modulation.

Interleukin-2 (IL-2) is an important cytokine signalling molecule in the immune system, but its marked systemic toxicity at high doses limits its clinical uses[1]. The surface presentation of IL-2 on biomaterials may prolong its half-life and minimize its systemic toxicity through local administration[42]. Here, we validated this approach as an alternative to the standard protocol of supplementing free IL-2 in media for ex vivo T cell culture[32]. We presented IL-2 on the surface of ICEp via its antibody clone #5355, which was engineered to facilitate the binding of IL-2 to its β and γ receptor on T cells, thus promoting the proliferation of non-T_{reg} T cells[46] (Fig. 5j). Using ICEp-bound IL-2 supplemented in the medium (0.005 OD_{550} ICEp carrying 0.57 ng ml^{-1} IL-2, Supplementary Fig. 6j) after ICEp-anti-CD3/CD28-[3:1]-mediated activation, significantly higher folds of cell expansion (at day 14) than an equivalent amount of free IL-2 supplementation (0.54 ng ml^{-1}) for both CD4+ and CD8+ T cells were observed across four independent T-cell donors (Fig. 5k,l, $P = 0.0001$ for CD4+ and $P = 0.0024$ for CD8+). Importantly, the higher fold of expansion with ICEp-bound IL-2 supplementation did not lead to a higher level of exhaustion for both CD4+ and CD8+ T cells (Fig. 5m). We observed similar levels of CD4+ and CD8+ cell expansion between the standard protocol with free IL-2 and approximately tenfold less ICEp-bound IL-2 (Supplementary
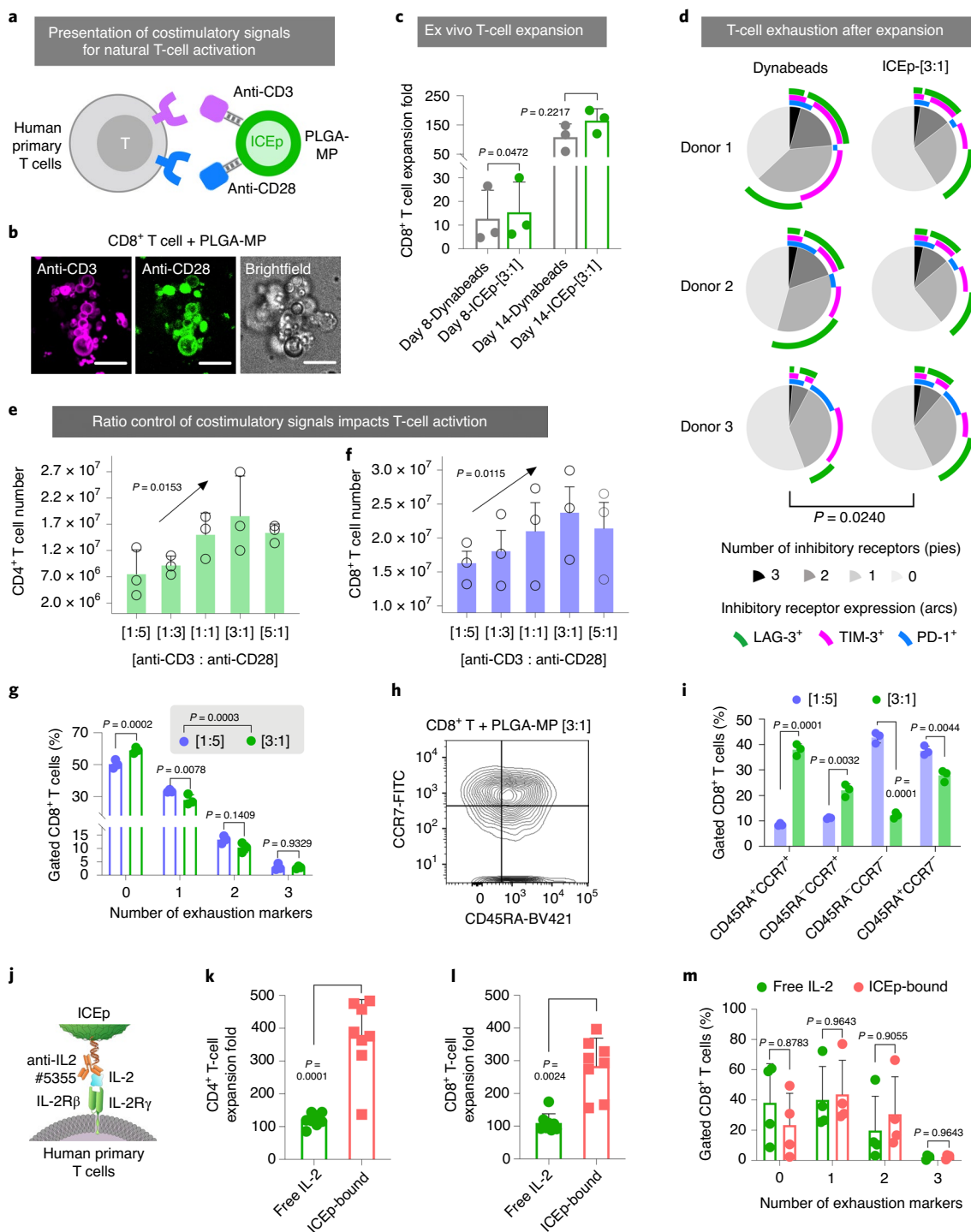

Fig. 5 | ICEp, capable of versatile and precisely controlled modulatory signals, regulates T cell characteristics during ex vivo expansion. a, Schematic of ICEp (PLGA microparticles with anti-CD3 and anti-CD28 antibodies controlled at specific ratios by DNA scaffolds, for example, [1:5] to [5:1]) triggering human primary T-cell activation and expansion. **b**, Representative confocal microscopy images of human primary CD8+ T cells co-incubated with ICEp-[1:1] overnight, showing ICEp-induced cell clumps ($n = 3$ biologically independent samples). Scale bar, 10 μm. **c**, Cell yield of human primary CD8+ T cells 8 and 14 days after activation by ICEp-[3:1], compared to commercially available Dynabeads. Data are mean ± s.d. and P values were determined by two-tailed paired t-test ($n = 3$ independent donors of two independent experiments). **d**, Exhaustion marker analysis of CD8+ T cells after stimulation with ICEp-[3:1] or Dynabeads for 14 days. The P value was determined by nested one-way ANOVA analysis of cell population with 0 to 3 inhibitory receptors between ICEp-[3:1] and Dynabeads activation. **e,f**, Cell yield of human primary CD4+ (**e**) and CD8+ (**f**) T cells 14 days after activation of 1.4×10^5 cells by ICEp with varying ratios of anti-CD3 to anti-CD28 ranging from [1:5] to [5:1]. Data are mean ± s.e.m. ($n = 3$ independent donors of two independent experiments) and P values were determined by one-way ANOVA test for linear trend. **g**, The population of CD8+ T cells with 0 to 3 inhibitory receptors after being stimulated by ICEp-[1:5] or ICEp-[3:1] for 14 days. Data are mean ± s.d. and P values were determined by multiple t-test for comparison of 0–3 subgroups and nested one-way ANOVA analysis for comparison between treatments of ICEp-[1:5] and ICEp-[3:1] ($n = 3$ independent donors of two independent experiments). **h**, Representative two-dimensional dot plot of CCR7 and CD45RA expression on CD8+ T cells activated by ICEp-[3:1] for 7 days, and the gating strategy to analyse T-cell differentiation phenotype. **i**, CCR7 and CD45RA expression profile of CD8+ T cells stimulated by ICEp-[1:5] or ICEp-[3:1] for 7 days. Data are mean ± s.d. ($n = 3$ biological replicates from the same donor), and P values were determined by multiple t-test with correction using the Holm–Šidák method. **j**, Schematic of IL-2 presented on particles through its antibody (clone #5355) that exposes the epitope for β and γ units of its receptor on T cells, thus promoting T-cell proliferation. **k,l**, Cell expansion profile of primary CD4+ (**k**) and CD8+ (**l**) T cells stimulated by ICEp-[3:1] for 14 days with ICEp-bound IL-2 or free IL-2 supplemented at an equivalent dose. Data are mean ± s.d. ($n = 4$ independent donors of three independent experiments) and P values were determined by two-tailed paired t-test. **m**, The population of CD4+ and CD8+ T cells with 0 to 3 inhibitory receptors stimulated by ICEp-[3:1] for 14 days with ICEp-bound IL-2 or free IL-2 supplemented at an equivalent dose. Data are mean ± s.d. ($n = 4$ independent donors of three independent experiments) and P values were determined by multiple t-test with correction using the Holm–Šidák method.

Fig. 6k). This can be beneficial for both ex vivo T-cell expansion and local administration of IL-2-presenting ICEp at the tumour site to activate immune cells in vivo.

Conclusions

We demonstrated a unique platform using synthetic short DNA oligonucleotides as surface scaffolds on biodegradable materials for precise and controlled loading of multiple biomolecules at a specific ratio and density. A series of studies were carried out to achieve the maximum loading density, ratiometric control, adaptability to different particle sizes/composition and feasibility for use in vivo. We

demonstrated that: (1) a range of immune modulators (for example, antigen, costimulatory ligand, checkpoint inhibitor, cytokine) can be loaded on ICEp with intact bioactivity; (2) antigen-presenting ICEp can be administered locally to control AND-gate CAR-T cell activation and tumour clearance in vivo; and (3) the ratiometric control of costimulatory ligands (anti-CD3 and anti-CD28) and the presentation of IL-2 on ICEp surfaces can influence ex vivo T-cell activation and expansion. Through this highly modular platform, biocompatible materials can be employed as substrates for a wide spectrum of modulatory biomolecules, including cytokines[47], antigens[48], checkpoint inhibitors[13], agonistic or antagonistic anti-

bodies[49], adjuvants[50,51], etc., to regulate the local environment and enhance the efficacy of immune cells in cancer immunotherapy[52].

Online content

References

1. Riley, R. S., June, C. H., Langer, R. & Mitchell, M. J. Delivery technologies for cancer immunotherapy. *Nat. Rev. Drug Discov.* **18**, 175–196 (2019).
2. Lim, W. A. & June, C. H. The principles of engineering immune cells to treat cancer. *Cell* **168**, 724–740 (2017).
3. Chen, D. S. & Mellman, I. Oncology meets immunology: the cancer-immunity cycle. *Immunity* **39**, 1–10 (2013).
4. June, C. H. & Sadelain, M. Chimeric antigen receptor therapy. *N. Engl. J. Med.* **379**, 64–73 (2018).
5. Gajewski, T. F., Schreiber, H. & Fu, Y. X. Innate and adaptive immune cells in the tumor microenvironment. *Nat. Immunol.* **14**, 1014–1022 (2013).
6. Brudno, J. N. & Kochenderfer, J. N. Toxicities of chimeric antigen receptor T cells: recognition and management. *Blood* **127**, 3321–3330 (2016).
7. Riches, J. C. et al. T cells from CLL patients exhibit features of T-cell exhaustion but retain capacity for cytokine production. *Blood* **121**, 1612–1621 (2013).
8. Gust, J. et al. Endothelial activation and blood–brain barrier disruption in neurotoxicity after adoptive immunotherapy with CD19 CAR-T cells. *Cancer Discov.* **7**, 1404–1419 (2017).
9. Maus, M. V. et al. T cells expressing chimeric antigen receptors can cause anaphylaxis in humans. *Cancer Immunol. Res.* **1**, 26–31 (2013).
10. Sagiv-Barfi, I. et al. Eradication of spontaneous malignancy by local immunotherapy. *Sci. Transl. Med.* **10**, eaan4488 (2018).
11. Adachi, K. et al. IL-7 and CCL19 expression in CAR-T cells improves immune cell infiltration and CAR-T cell survival in the tumor. *Nat. Biotechnol.* **36**, 346–351 (2018).
12. Wallace, A. et al. Transforming growth factor-β receptor blockade augments the effectiveness of adoptive T-cell therapy of established solid cancers. *Clin. Cancer Res.* **14**, 3966–3974 (2008).
13. Rafiq, S. et al. Targeted delivery of a PD-1-blocking scFv by CAR-T cells enhances anti-tumor efficacy in vivo. *Nat. Biotechnol.* **36**, 847–856 (2018).
14. Tang, H. et al. Facilitating T cell infiltration in tumor microenvironment overcomes resistance to PD-L1 blockade. *Cancer Cell* **29**, 285–296 (2016).
15. Shah, N. J. et al. An injectable bone marrow-like scaffold enhances T cell immunity after hematopoietic stem cell transplantation. *Nat. Biotechnol.* **37**, 293–302 (2019).
16. Chen, Q. et al. In situ sprayed bioresponsive immunotherapeutic gel for post-surgical cancer treatment. *Nat. Nanotechnol.* **14**, 89–97 (2019).
17. Ye, Y. et al. A melanin-mediated cancer immunotherapy patch. *Sci. Immunol.* **2**, eaan5692 (2017).
18. Jiang, W. et al. Designing nanomedicine for immuno-oncology. *Nat. Biomed. Eng.* **1**, 0029 (2017).
19. Stephan, S. B. et al. Biopolymer implants enhance the efficacy of adoptive T-cell therapy. *Nat. Biotechnol.* **33**, 97–101 (2015).
20. Roybal, K. T. et al. Precision tumor recognition by T cells with combinatorial antigen-sensing circuits. *Cell* **164**, 770–779 (2016).
21. Brenner, M. J., Cho, J. H., Wong, N. M. L. & Wong, W. W. Synthetic biology: immunotherapy by design. *Annu. Rev. Biomed. Eng.* **20**, 95–118 (2018).
22. Yu, C. S., Xi, J. C., Li, M., An, M. & Liu, H. P. Bioconjugate strategies for the induction of antigen-specific tolerance in autoimmune diseases. *Bioconjug. Chem.* **29**, 719–732 (2018).
23. Shao, K. et al. Nanoparticle-based immunotherapy for cancer. *ACS Nano* **9**, 16–30 (2015).
24. Li, Y. & Kurlander, R. J. Comparison of anti-CD3 and anti-CD28-coated beads with soluble anti-CD3 for expanding human T cells: differing impact on CD8 T cell phenotype and responsiveness to restimulation. *J. Transl. Med.* **8**, 104 (2010).
25. Slifka, M. K. & Amanna, I. J. Role of multivalency and antigenic threshold in generating protective antibody responses. *Front. Immunol.* **10**, 956 (2019).
26. Hartwell, B. L. et al. Multivalent nanomaterials: learning from vaccines and progressing to antigen-specific immunotherapies. *J. Pharm. Sci.* **104**, 346–361 (2015).
27. Shaw, A. et al. Binding to nanopatterned antigens is dominated by the spatial tolerance of antibodies. *Nat. Nanotechnol.* **14**, 398–398 (2019).
28. Shi, B. Y. et al. Challenges in DNA delivery and recent advances in multifunctional polymeric DNA delivery systems. *Biomacromolecules* **18**, 2231–2246 (2017).
29. Sapsford, K. E. et al. Functionalizing nanoparticles with biological molecules: developing chemistries that facilitate nanotechnology. *Chem. Rev.* **113**, 1904–2074 (2013).
30. Iyisan, B. & Landfester, K. Modular approach for the design of smart polymeric nanocapsules. *Macromol. Rapid Commun.* **40**, e1800577 (2019).
31. Huang, X., Lai, Y. F., Braun, G. B. & Reich, N. O. Modularized gold nanocarriers for TAT-mediated delivery of siRNA. *Small* **13**, 1602473 (2017).
32. Cheung, A. S., Zhang, D. K. Y., Koshy, S. T. & Mooney, D. J. Scaffolds that mimic antigen-presenting cells enable ex vivo expansion of primary T cells. *Nat. Biotechnol.* **36**, 160–169 (2018).
33. Zhou, J., Patel, T. R., Fu, M., Bertram, J. P. & Saltzman, W. M. Octa-functional PLGA nanoparticles for targeted and efficient siRNA delivery to tumors. *Biomaterials* **33**, 583–591 (2012).
34. Douglas, S. M., Bachelet, I. & Church, G. M. A logic-gated nanorobot for targeted transport of molecular payloads. *Science* **335**, 831–834 (2012).
35. Stephanopoulos, N. Hybrid nanostructures from the self-assembly of proteins and DNA. *Chem* **6**, 364–405 (2020).
36. Hu, Y. & Niemeyer, C. M. From DNA nanotechnology to material systems engineering. *Adv. Mater.* **31**, e1806294 (2019).
37. Wang, S. et al. DNA-functionalized metal–organic framework nanoparticles for intracellular delivery of proteins. *J. Am. Chem. Soc.* **141**, 2215–2219 (2019).
38. Peterson, A. M. & Heemstra, J. M. Controlling self-assembly of DNA–polymer conjugates for applications in imaging and drug delivery. *Wiley Interdiscip. Rev. Nanomed. Nanobiotechnol.* **7**, 282–297 (2015).
39. Wang, Z. G., Li, N., Wang, T. & Ding, B. Surface-guided chemical processes on self-assembled DNA nanostructures. *Langmuir* **34**, 14954–14962 (2018).
40. Allahyari, M. & Mohit, E. Peptide/protein vaccine delivery system based on PLGA particles. *Hum. Vaccin. Immunother.* **12**, 806–828 (2016).
41. Schmid, D. et al. T cell-targeting nanoparticles focus delivery of immunotherapy to improve antitumor immunity. *Nat. Commun.* **8**, 1747 (2017).
42. Zamecnik, C. R., Lowe, M. M., Patterson, D. M., Rosenblum, M. D. & Desai, T. A. Injectable polymeric cytokine-binding nanowires are effective tissue-specific immunomodulators. *ACS Nano* **11**, 11433–11440 (2017).
43. Blanco, E., Shen, H. & Ferrari, M. Principles of nanoparticle design for overcoming biological barriers to drug delivery. *Nat. Biotechnol.* **33**, 941–951 (2015).
44. Rodriguez, P. L. et al. Minimal 'self' peptides that inhibit phagocytic clearance and enhance delivery of nanoparticles. *Science* **339**, 971–975 (2013).
45. Gattinoni, L. et al. A human memory T cell subset with stem cell-like properties. *Nat. Med.* **17**, 1290–1297 (2011).
46. Arenas-Ramirez, N. et al. Improved cancer immunotherapy by a CD25-mimobody conferring selectivity to human interleukin-2. *Sci. Transl. Med.* **8**, 367ra166 (2016).
47. Tang, L. et al. Enhancing T cell therapy through TCR-signaling-responsive nanoparticle drug delivery. *Nat. Biotechnol.* **36**, 707–716 (2018).
48. Singha, S. et al. Peptide–MHC-based nanomedicines for autoimmunity function as T-cell receptor microclustering devices. *Nat. Nanotechnol.* **12**, 701–710 (2017).
49. Huang, B. et al. Active targeting of chemotherapy to disseminated tumors using nanoparticle-carrying T cells. *Sci. Transl. Med.* **7**, 291ra294 (2015).
50. Smith, T. T. et al. In situ programming of leukaemia-specific T cells using synthetic DNA nanocarriers. *Nat. Nanotechnol.* **12**, 813–820 (2017).
51. Kuai, R., Ochyl, L. J., Bahjat, K. S., Schwendeman, A. & Moon, J. J. Designer vaccine nanodiscs for personalized cancer immunotherapy. *Nat. Mater.* **16**, 489–496 (2017).
52. Wang, C., Ye, Y., Hu, Q., Bellotti, A. & Gu, Z. Tailoring biomaterials for cancer immunotherapy: emerging trends and future outlook. *Adv. Mater.* **29**, 1606036 (2017).

Methods

Synthesis of thiol-modified DNA. 3′-Thiol-modified DNA was synthesized on 3′-thiol-modifier 6 S-S CPG beads (Glen Research, catalogue no. 10-1936-02) using an Expedite 8909 DNA synthesizer. DNA oligonucleotides were retrieved from the beads by incubation at 70 °C for 20 min in the presence of AMA solution (ammonium hydroxide:methylamine, 1:1, v/v), followed by vacuum evaporation (SpeedVac, ThermoFisher, catalogue no. SPD121P-230) for 3 h to remove AMA. DNA oligonucleotides were reconstituted in TE buffer (Tris–EDTA, 10 mM, pH 7.5), then filtered through a 0.22-µm filter (Millipore, catalogue no. UFC30GV00) and stored at −20 °C.

Synthesis of polymer–DNA amphiphilic molecule. 3′-Thiol-modified DNA oligonucleotides were deprotected through treatment with a 100× molar excess of tris(2-carboxyethyl)phosphine hydrochloride solution (TCEP, Sigma, catalogue no. 646547) at 37 °C for 1 h, and purified by size-exclusion chromatography (Glen Research, catalogue no. 61-5010). Unless otherwise specified, freshly prepared thiol-DNA 17mer at 200 µM were reacted with poly(lactide-co-glycolide)-*b*-poly(ethylene glycol)-maleimide (M_w = 10,000:5,000 Da, PLGA10k-PEG5k-Mal, Akina, catalogue no. AI053) at a 1:1 ratio in a solvent composed of dimethylformamide (DMF)/H_2O (90:10, v/v) and 0.2% triethanolamine and incubated at room temperature overnight. The next day, the solvent was removed by vacuum evaporation at 70 °C for 3 h, and the dried mixture was stored at −20 °C. The product was verified by TBE–urea gel electrophoresis (15%, ThermoFisher, catalogue no. EC68855) with SYBR gold dye staining (ThermoFisher, catalogue no. S11494), and the conjugation efficiency was quantified by gel densitometry analysis using GelQuantNET v.1.8 software.

Fabrication of polymeric particles with DNA. To fabricate PLGA particles of varying sizes (Supplementary Fig. 2j), the dried polymer–DNA reaction mixture (from 100 nmol of each reactant) reconstituted in 200 µl of solvent (ethyl acetate:H_2O, 1:1, v/v) was incorporated into a mixture containing 0.5 ml of ethyl acetate (EtOAc), a certain amount of unmodified polymer (poly-lactic-co-glycolic acid, 50:50, M_w = 38,000–54,000 Da, Sigma, catalogue no. 719900) and 0.5 or 1.0 ml of aqueous buffer (10 mM sodium citrate, 600 mM Na^+, pH 3.0), which either included or did not include 1% polyvinyl alcohol (PVA, Sigma, catalogue no. 81381). The whole mixture was then vortexed and probe-sonicated (Fisher miniRoto S56) on ice at 7–8 W for 5 × 5 s with 10-s intervals. After sonication, the mixture was immediately combined with 9 ml of 0.2% PVA and stirred in a chemical hood for 3 h so that the ethyl acetate could evaporate. Particles were then filtered through a 40-µm cell strainer (Sigma, catalogue no. CLS431750) and washed through centrifugation at 10,000g for 10 min. The pellet was then resuspended in TE buffer (10 mM Tris–HCl, pH 8.0) with 0.01% Tween-20 added. This washing protocol remained the same for later fabrications. After three washes, particles were suspended in TE buffer with 1% PVA and lyophilized (VirTis Advantage Plus) for long-term storage. The size profile of particles was characterized by dynamic light scattering with a Malvern Nano ZS instrument and scanning electron microscopy (SEM) imaging using a Zeiss Ultra-55 scanning electron microscope. The particle concentration was normalized using the optical density at 550 nm (OD_{550}) measured using an ultraviolet–visible spectrometer (Molecular Devices SpectraMax M5).

The same fabrication protocol was used for PLA microparticles, but the emulsion mixture was adjusted: 0.5 ml of dichloromethane (DCM) with 100 mg ml^{-1} poly(lactic acid) (M_w = 60,000 Da, Sigma, catalogue no. 38534), 0.5 ml of aqueous buffer (10 mM sodium citrate, 600 mM Na^+, 0.3% PVA, pH 3.0) and the polymer–DNA reaction (from 200 nmol of each reactant) reconstituted in 200 µl of solvent (ethyl acetate:H_2O, 1:1, v/v). To encapsulate biomolecules in the core of DNA-scaffolded particles another emulsion step was added before the above emulsion: biomolecules, including 0.25 mg of fluorescein isothiocyanate (FITC)-labelled peptide with 21 amino acids (LifeTein) and 50 nmol of 5′-Cy3-labelled DNA 21mer (Bioresearch Technologies) dissolved in 50 µl of PBS (pH 7.0) was mixed into the 0.5 ml of ethyl acetate solution with dissolved PLGA (Sigma, catalogue no. 719900) and probe-sonicated at 7–8 W for 5 × 5 s with 10-s intervals on ice. Immediately after this, the amphiphilic polymer–DNA and an aqueous buffer were added following the same protocol described above.

Attachment of complementary DNA to proteins and their purification. IgG antibodies were attached to complementary DNA strands through the TCEP strategy. Various modified complementary DNA strands were all from Biosearch Technologies. Antibodies were first exchanged in reducing buffer (PBS with 10 mM EDTA) by size-exclusion chromatography (Zeba Spin Desalting Column, ThermoFisher, catalogue no. 89882), and the disulfide bond at the hinge region was selectively reduced through the addition of TCEP at a 3 molar or 4.5 molar excess and subsequent incubation at 37 °C for 1 h. Excess TCEP was removed through size-exclusion chromatography. 3′-Amine-modified complementary DNA was conjugated to a MAL-dPEG4-NHS linker (Quanta Biodesign, catalogue no. 10214) with a 30-fold molar excess in HEPES buffer (pH 7.0) at 37 °C for 1 h, followed by the removal of the unconjugated linker through a 70% ethanol precipitation and size-exclusion chromatography. The reduced antibody and modified DNA were combined at a 1:10 molar ratio and incubated at 37 °C for 1 h then 4 °C overnight.

The next day, DNA–protein conjugates were purified using protein G affinity chromatography (Genscript, catalogue no. L00209) to remove unconjugated DNA.

The anti-PD-L1 (Bio X Cell, catalogue no. BE0285) antibody was conjugated to 3′-NH_2-5′-Quasar570-modified DNA 22-mer through a HyNic-4FB linker (TriLink, catalogue no. S-9011) following the kit's instructions. As a validation of the antibody activity post-conjugation, purified anti-PD-L1–DNA conjugates from the 'TCEP' strategy and the TriLink strategy and PE anti-human PD-L1 (Biolegend, catalogue no. 329705, 1:500 dilution) were incubated with PD-L1-overexpressing K562 cells at 4 °C for 30 min, followed by two washes (centrifugation at 400g for 5 min and resuspension in PBS) for flow cytometry with a BD LSR II. Anti-PD-L1–DNA conjugates linked through the 'TCEP' strategy were loaded onto DNA-scaffolded PLGA microparticles. PD-L1-overexpressed and wild-type K562 cells at 1 million per ml were added to particles at 0.3 OD_{550} and incubated for 30 min at 37 °C, followed by cell nuclei staining with Hoechst 33342 (ThermoFisher, catalogue no. 62249). Imaging was performed using the spinning disk confocal fluorescence microscope (Nikon Yokogawa CSU-22).

His-tag GFP was expressed by *Escherichia coli* BL21 (DE3) (Novagen) transduced with pRSET-EmGFP vector (ThermoFisher, catalogue no. V35320) in *E. coli* expression medium (MagicMedia, Invitrogen, catalogue no. K6803). His-tag GFP was extracted using cell lysis reagent (Sigma, catalogue no. B7435) then purified using nickel-nitrilotriacetic acid affinity chromatography (Invitrogen, catalogue no. R90115). The MAL-PEG4-NHS linker (Quanta Biodesign) was mixed with GFP at a 30-fold molar excess and incubated at 37 °C for 1 h; size-exclusion chromatography was then used to remove the excess linker. 3′-Thiol-modified complementary DNA was decapped using the protocol described above and reacted with modified GFP at a 1:10 molar ratio at 37 °C for 1 h then at 4 °C overnight. The next day, GFP-DNA conjugates were purified using nickel-nitrilotriacetic acid affinity chromatography to remove unconjugated DNA. Protein–DNA conjugates were analysed through SDS–PAGE gel electrophoresis (Genscript, catalogue no. M42012L) with SYPRO Ruby dye staining (ThermoFisher, catalogue no. S21900).

Ratiometric control of surface DNA scaffolds with different sequences and the co-loading of versatile payloads. 3′-Thiolated DNA with different sequences was synthesized, namely R, G and B (Supplementary Fig. 2a). Following the conjugation with PLGA10k-PEG5k-Mal (Akina, catalogue no. AI053), polymer–DNA molecules from different sequences were mixed at varying ratios and incorporated into the particle fabrication process described above (100 nmol for each reactant). Strands complementary to the DNA scaffolds that were pre-conjugated with small molecules (for example, fluorescent dye or biotin, at 1 µM per OD_{550}) or proteins (for example, GFP or antibodies at 180 nM per OD_{550}) were incubated with particles at 37 °C for 30 min in PBS buffer with 600 mM of Na^+ and 0.01% Tween-20 supplemented for the surface hybridization of payloads. The excess was removed by three washes. For co-loading of multiple cargos, the input proportion of each individual strand with a specific sequence was consistent with its DNA–polymer counterpart input during the particle fabrication. To control GFP density on DNA-scaffolded particles, an excess amount of complementary DNA-GFP conjugates were hybridized to particles with a corresponding scaffold sequence determined at different densities (for example 1/3, 1/2 or full in Fig. 4d). Another method of adjusting the density of GFP was the hybridization of full-density DNA-scaffolded particles with complementary DNA-GFP at varying concentrations (for example 15 nM per OD, 30 nM per OD, 60 nM per OD and 180 nM per OD in Fig. 4e).

The loading efficiencies of different cargos on the surface or in the core were quantified through a fluorescence-based assay using dye-labelled DNA strands (5′-Quasar570-compR, 5′-FITC-compG, 5′-Quasar705-compG, 5′-Quasar670-compB, Supplementary Fig. 2a), peptides (C terminus FITC-labelled peptide, LifeTein) or proteins (FITC-labelled human IgG, Sigma, catalogue no. SLBW7799) after etching the particles with DMSO and diluting with 9× volume of water. The fluorescence signal was detected by a plate reader (Tecan Spark with Tecan SparkControl Software v.2.1) and analysed using a calibration curve normalized from OD_{550}. Functionalized microparticles with fluorescent labels were imaged through a spinning disk confocal fluorescence microscope (Nikon Yokogawa CSU-22 with NIS Elements AR 5.21.00_b1483), and the size distribution was quantified using ImageJ software analysis from acquired images. Fluorescent microparticles were also analysed for concentration using a cell counter (Countess II FL AMQAF1000, ThermoFisher).

Loading of biotinylated biomolecules on streptavidin-coated microparticles and the ratiometric control. To conjugate streptavidin onto the surface of particles with maleimide functional groups, streptavidin (Prozyme, catalogue no. SA10) was reacted with an SPDP (*N*-succinimidyl 3-(2-pyridyldithio)propionate) linker (Sigma, catalogue no .P3415) at a 20-fold molar excess in HEPES buffer (pH 7.0) at 37 °C for 1 h. The size-exclusion chromatography was then used to remove excess SPDP and exchange to the reducing buffer (PBS with 10 mM EDTA). A 30-fold molar excess of TCEP was then added to reduce streptavidin-SPDP to free thiols. This mixture was incubated at 37 °C for 1 h, then added onto maleimide-presenting particles at 1.0 mg ml^{-1} per OD_{550}. The mixture containing streptavidin-SPDP and particles was incubated at 37 °C for 1 h, then the particles were washed three times.

To load biotinylated DNA on streptavidin-coated particles, DNA strands with different fluorescent labels (5′-FITC-compG-3′-biotin, 5′-Quasar705-compG-3′-biotin and 5′-Quasar570-compR-3′-biotin) were individually added or mixed at certain molar ratios to particles with a total of 180 nM per OD_{550}. The mixture was incubated at room temperature for 30 min so that the DNA can bind with streptavidin on the surface of the particles, then the particles were washed three times. Particles were dissolved by DMSO, and the fluorescence signal was analysed using the plate reader as described above.

For the biotin-modification of proteins, GFP was reacted with a 10× molar excess of NHS-PEG$_4$-biotin (Quanta Biodesign, catalogue no. 10200) in NaHCO$_3$ buffer (10 mM, pH 8.0) for 1 h at 37 °C; IgG antibodies were reduced using the TCEP strategy as described above and were reacted with 10× molar excess of MAL-PEG$_3$-biotin (Quanta Biodesign, catalogue no. 10201) in PBS buffer with 10 mM EDTA for 1 h at 37 °C. The excess biotin was removed through two rounds of purification with size-exclusion chromatography, and then the protein concentration was quantified using a spectrophotometer. The biotinylated antibodies were further fluorescently labelled through a reaction with NHS-AFDye555 (Click Chemistry Tools, catalogue no. 1341) or NHS-Cy5 (Lumiprobe, catalogue no. 13020) with an 8× molar excess at 37 °C for 1 h. To remove the unconjugated dye, the biotinylated antibodies were then purified twice using size-exclusion chromatography. The protein concentration was also determined by spectrophotometer quantification. Modified proteins (biotin-GFP, biotin-IgG-Cy5 and biotin-IgG-AF555) were added individually or mixed at specific molar ratios to streptavidin-coated particles at 0.1 mM total per OD_{550} with 1% BSA/PBS. After an incubation at room temperature for 30 min, the particles were washed twice. Particles were analysed by fluorescence signal using the plate reader, and the signals were normalized to OD_{550}.

Antigen-binding activity of anti-PD-L1 antibody-loaded particles. PLGA microparticles assembled with anti-PD-L1 antibodies were added to an excess amount of biotinylated human PD-L1 (4 μg ml^{-1} per OD_{550}, Sino Biological, catalogue no. 10084-H08H-B, or Acro Biosystems, catalogue no. PD1-H82E5) in 1% BSA/PBS. The mixture underwent an incubation at room temperature for 30 min, then the particles were washed twice. In a separate reaction, streptavidin was fluorescently labelled with FITC or AFDye555 dye through reaction with an 8× molar excess of NHS-FITC (ThermoFisher, catalogue no. 46409) or NHS-AFDye555 (Click Chemistry Tools, catalogue no. 1341) in NaHCO$_3$ buffer (10 mM, pH 8.0) for 30 min at 37 °C. Afterwards, the fluorescently labelled streptavidin was purified twice via size-exclusion chromatography (Glen Research, catalogue no. 61-5010) to remove the unconjugated dye. A large excess of fluorescently labelled streptavidin (~150 μg ml^{-1} per OD_{550}) was added to biotinylated PD-L1-bound particles in 1% BSA/PBS and incubated at room temperature for 30 min, and then the particles were washed twice. Particles were imaged using the spinning disk confocal fluorescence microscope (Nikon Yokogawa CSU-22), and images were analysed using ImageJ software, which detects the mean fluorescence intensity (MFI) of particles.

Traditional surface step-by-step conjugation for attaching payload. To attach thiol-modified biomolecules or IgG antibodies onto particles without DNA scaffolds, particles with maleimide functional groups on the surface were fabricated with all of the steps of above protocol, with replacement of the polymer–DNA reaction mixture by 100 nmol PLGA-PEG-MAL (Akina, catalogue no. AI053). Freshly prepared particles with maleimide functional groups were then reacted with either 3′-thiol-5′-Quasar670-modified DNA at 1 μM per OD_{550} or reduced antibodies with free thiols (FITC-IgG, Sigma) at 180 nM per OD_{550} for 1 h at 37 °C, then at 4 °C overnight. The next day particles were washed and quantified through the fluorescence-based analysis.

To conjugate IgG molecules onto the surface of particles using DNA scaffolds, particles were first hybridized with 3′-amine-modified complementary DNA strands at 1 μM per OD_{550}, then washed three times. A large excess of the MAL-dPEG4-NHS linker (Quanta Biodesign) was added at 30 μM per OD_{550} and incubated at room temperature for 1 h, then washed three times to bring maleimide functional groups onto DNA scaffolds. Reduced antibodies with free thiols (FITC-IgG, Sigma) were conjugated to the maleimide groups using the above protocol.

To conjugate GFP to the functional groups presented by DNA scaffolds, particles were hybridized with 3′-thiol-modified complementary DNA strands at 1 μM per OD_{550} and decapped by TCEP with the above protocol, then washed three times. The MAL-PEG4-NHS linker (Quanta Biodesign) was mixed with GFP at a 100-fold molar excess, incubated at 37 °C for 1 h and then the excess was removed via size-exclusion chromatography. Freshly prepared particles and ~300 nM per OD_{550} linker-attached GFP were combined and reacted at room temperature for 1 h, then washed three times.

Stability test in DNase and human serum. To test the stability of DNA scaffolds, PLGA microparticles were hybridized with fluorescently labelled complementary DNA strands, then loaded with human FITC-IgG (Sigma, catalogue no. SLBW7799) through surface step-by-step conjugation. Particles with and without IgG coverage were suspended in the enzyme reaction buffer (Promega, catalogue no. M6101)

plus DNase (RQ1 RNase-free DNase, Promega, catalogue no. M6101) at 5 U per 1 OD_{550} × 50 μl and incubated at 37 °C for 20 min. Then, a stop buffer was added (Promega, catalogue no. M6101) and the mixture was centrifuged at 10,000 g for 10 min to collect the supernatant and pellet for the fluorescence-based analysis. Similarly, particles with and without IgG attachment, together with particles hybridized by GFP-DNA conjugates, were suspended in human serum (bioWORLD, catalogue no. v13081400) and incubated for 1 h at 37 °C, then centrifuged to collect the supernatant and pellet for the fluorescence-based analysis.

To test the serum stability of particles, an NH$_2$-modified PLGA polymer (LG 50:50, M_w = 30,000–40,000 Da) or an NH$_2$-modified PLA polymer (Akina, catalogue no. AI19, M_w = 40,000 Da), dissolved in DMF, was reacted with a Cyanine3 (Cy3)-NHS ester (Lumiprobe, catalogue no. 11020) at a 30-fold molar excess at room temperature for 1 h, then the mixture repeatedly underwent 70% ethanol precipitation and DMF re-dissolution to remove the unconjugated dye. The Cy3-labelled polymer (1 mg) was incorporated into the emulsion protocol for DNA-scaffolded (G strand) microparticles. Particles were suspended in human serum (bioWORLD, catalogue no. v13081400) and incubated at 37 °C over 14 days, with aliquots being sampled for the fluorescence-based analysis as described above.

Cell lines and culture. K562 human myelogenous leukaemia cells (ATCC, catalogue no. CCL-243) and A375 human malignant melanoma cells (ATCC, catalogue no. CRL-1619) were used in T cell killing experiments. K562 and A375 were lentivirally transduced to stably express human HER2, PD-L1 and GFP. All cell lines were fluorescence activated cell sorted (FACS) for expression of the transgenes. Murine pro-B cell line BA/F3 (DSMZ, catalogue no. ACC 300), T cell lymphoma line EL4 (DSMZ, catalogue no. ACC 831) and bone marrow line 32D (DSMZ, catalogue no. ACC 411) were used to test synthetic circuit activation in mouse cells. BA/F3 and 32D cell lines were cultured in RPMI 1640 (ThermoFisher, catalogue no. 11875085) with 10% fetal bovine serum (FBS, UCSF Cell Culture Facility), 10 ng ml^{-1} mouse IL-3 (ThermoFisher, catalogue no. PMC0035) and penicillin–streptomycin (Sigma, catalogue no. P4333). The EL4 cell line was cultured in RPMI 1640 (ThermoFisher, catalogue no. 11875085) with 5% FBS (UCSF Cell Culture Facility) and penicillin–streptomycin (Sigma, catalogue no. P4333). A murine macrophage cell line J77A4.1 (ATCC, catalogue no. TIB-67) was used for the particle-uptake assay. K562 cells were cultured in Iscove's Modified Dulbecco's Medium (Corning, catalogue no. 10-016-CV) with 10% FBS (UCSF Cell Culture Facility) and gentamicin (UCSF Cell Culture Facility). A375, J77A4.1 cells and Lenti-X 293T packaging cells (Clontech, catalogue no. 11131D) were cultured in DMEM (Gibco, catalogue no. 10569-010) with 10% FBS. All cell lines in this work were tested negative for mycoplasma contamination.

Macrophage uptake assay. The biotin-modified 'self' peptide (biotin-miniPEG-GNYTCEVTELTREGETIIELK[Lys(FITC)], LifeTein) was loaded onto streptavidin-tethered PLGA microparticles using the protocol described above. The streptavidin on the control particles without the 'self' peptide was labelled with NHS-fluorescein (ThermoFisher, catalogue no. 46409) at 6 μM per OD_{550} for 1 h at room temperature, then washed three times. The murine macrophage cell line J77A4.1 (ATCC) grown on glass-bottomed chamber slides (Thermo Scientific, catalogue no. 154526) was treated with lipopolysaccharides (Sigma, catalogue no. L4391) at 100 ng ml^{-1} overnight. The next day, 'self' peptide-loaded particles and control particles were added at 0.03 OD_{550} × 200 μl and incubated at 37 °C for 1 h. Cells were then washed three times with PBS to remove non-internalized particles, and then they were fixed using 4% paraformaldehyde (Electron Microscopy Sciences, catalogue no. 15710) for 20 min. After three washes, cells were imaged using the spinning disk confocal fluorescence microscope (Nikon Yokogawa CSU-22). Images were analysed for cell fluorescence signals using ImageJ v.2.0.0 software.

Primary human T-cell isolation and culture. Blood was obtained from Blood Centers of the Pacific as approved by the University Institutional Review Board. Primary CD4$^+$ and CD8$^+$ T cells were isolated from anonymous donor blood samples after apheresis by negative selection (STEMCELL Technologies, catalogue nos 15062 and 15063). T cells were cryopreserved in RPMI 1640 (Corning, catalogue no. 10-040-CV) with 20% human AB serum (Valley Biomedical, catalogue no. HP1022) and 10% DMSO. After thawing, T cells were cultured in human T-cell medium consisting of X-VIVO 15 (Lonza, catalogue no. 04-418Q), 5% human AB serum and 10 mM neutralized N-acetyl-ʟ-cysteine (Sigma-Aldrich, catalogue no. A9165) supplemented with 30 units ml^{-1} of IL-2 (NCI BRB Preclinical Repository) for all experiments.

Antibody staining and flow cytometry analysis. All antibody staining for flow cytometry was carried out in the wells of round-bottomed 96-well tissue culture plates. The plates were centrifuged for 4 min at 400 g, resulting in pelleting of the cells. The supernatant was removed, and the cells were resuspended in 50 μl of PBS containing the fluorescent antibody of interest. Cells were stained after 25 min at 4 °C in the dark. Stained cells were then washed twice with PBS and resuspended in fresh PBS for flow cytometry with a BD LSR II or a BD LSRFortessa. All flow cytometry data were collected using BD FACSDiva Software v.8.0.1 and the analysis was performed in FlowJo software v.10.7.1.

ICEp-mediated activation of human primary T cells for ex vivo activation.
Anti-CD3/CD28 ICEp were synthesized using PLGA microparticles functionalized with anti-CD3 antibodies (Bio X Cell, catalogue no. BE0001-2, attached to 3′-NH$_2$-5′-Quasar670-modified compB) and anti-CD28 antibodies (Bio X Cell, catalogue no. BE0248, attached to 3′-NH$_2$-5′-FAM-modified compR) at varying ratios, including 1:5, 1:3, 1:1, 3:1 to 5:1, according to the method described above. After thawing and a 24-hour recovery in culture, 1.4×10^5 CD4$^+$/CD8$^+$ human primary T cells in 200 µl of medium were added to ICEp at 0.11OD$_{550}$ (approximately 2.5 ICEp to 1 cell) or to CD3/CD28 Dynabeads at a 1:2.5 cell:bead ratio (Life Technologies, catalogue no. 11131D) for 4 days. CD8$^+$ T cells were imaged through the spinning disk confocal microscope (Nikon Yokogawa CSU-22) 0, 1, 8 and 14 days after ICEp addition. Dynabeads were removed using the magnetic plate 5 days after the cells were stimulated, whereas ICEp were not removed. CD4$^+$ and CD8$^+$ T-cell numbers were quantified using a cell counter (Countess II FL AMQAF1000, ThermoFisher) every other day from day 6 to day 14 after ICEp activation. Medium containing fresh IL-2 was supplemented to maintain the cell concentration between 0.5 and 1.5 million per ml. T-cell differentiation (day 7) and exhaustion (day 14) phenotypes were studied by flow cytometry analysis using the following antibodies: anti-CCR7 (BD, catalogue no. 561271, 1:20 dilution, and Biolegend, catalogue no. 353226, 1:200 dilution), anti-CD45RA (BD, catalogue no. 562885, 1:100 dilution, and Biolegend, catalogue no. 304150, 1:200 dilution), anti-CD45RO (BD, catalogue no. 564291, 1:200 dilution), anti-CD62L (Biolegend, catalogue no. 304830, 1:200 dilution), anti-CD27 (Biolegend, catalogue no. 356424, 1:200 dilution), anti-CD95 (Biolegend, catalogue no. 305644, 1:200 dilution), anti-LAG-3 (BD, catalogue no. 565720, 1:25 dilution), anti-TIM-3 (BD, catalogue no. 565558, 1:25 dilution) and anti-PD-1 (Biolegend, catalogue no. 329936, 1:25 dilution).

The anti-IL-2 clone no. 5355 (ThermoFisher, catalogue no. MA523696) was biotinylated using NHS-PEG$_4$-biotin (Quanta Biodesign, catalogue no. 10200) at a 30-fold molar excess. The mixture was incubated at 37 °C for 1 h, then purified via size-exclusion chromatography (ThermoFisher, catalogue no. 89882). Streptavidin-tethered PLGA microparticles were incubated with biotinylated anti-IL-2 at 20 nM per OD$_{550}$ and IL-2 (NCI BRB Preclinical Repository) at 1.5 or 30 nM per OD$_{550}$ at room temperature for 30 min and washed twice. IL-2-loaded ICEp were added to IL-2-free T-cell medium to obtain a final particle concentration of 0.005 OD$_{550}$ and ICEp-[3:1]-treated T cells were replenished with this medium to maintain the cell concentration at 0.5–1.5 million per ml. As a comparison to free IL-2 supplementation at 30 units ml^{-1} (0.54 ng ml^{-1}), ICEp from 30 nM per OD$_{550}$ IL-2 incubation (yield 114.0 ng ml^{-1} per OD$_{550}$, 0.57 ng ml^{-1} in the medium, Supplementary Fig. 6g) was equivalent to free IL-2, while ICEp from 1.5 nM per OD$_{550}$ incubation (yield 9.8 ng ml^{-1} per OD$_{550}$, 0.049 ng ml^{-1} in the medium, Supplementary Fig. 6g) was about 10-fold less than free IL-2 supplementation.

Transduction of synthetic circuit in human primary T cells and murine cell lines. For the transduction of human primary T cells, the binding domain of the LaG17 nanobody[20] was cloned into synNotch receptors with the Gal4 DNA-binding domain, VP64, as a synthetic transcription factor[20]. The response element plasmids were modified from the pHR′SIN:CSW vector with five copies of the Gal4 DNA-binding domain, a HER2 CAR in the multiple cloning site downstream of the Gal4 response elements and a PGK promoter that constitutively drives mCherry expression to easily identify transduced T cells[20]. All constructs were cloned via InFusion cloning (Takara Bio, catalogue no. 638910). A pantropic VSV-G pseudotyped lentivirus was produced via transfection of Lenti-X 293T cells with a pHR′SIN:CSW transgene expression vector and viral packaging plasmids pCMVdR8.91 and pMD2.G using Fugene HD (Promega, catalogue no. E2312). Human primary T cells were thawed the same day and, after 24 h in culture, were stimulated with Human T-Activator CD3/CD28 Dynabeads (Life Technologies, catalogue no. 11131D) at a 1:2.5 cell-to-bead ratio. At 48 h, the viral supernatant was collected, and the primary T cells were exposed to the virus for 24 h. At day 5 after T-cell stimulation, Dynabeads were removed and the T cells expanded until day 12 when they were rested and could be used in assays. T cells were sorted for assays with a BD FACSAria II on day 5 post-T-cell stimulation.

For murine immune cell lines 32D, BA/F3 and EL4, a LaG17-synNotch receptor and response element vector, were transduced using a lentivirus using the same protocol mentioned above. Differently, the response element vector plasmids were modified from the pHR′SIN:CSW vector with five copies of the Gal4 DNA-binding domain target sequence 5′ to a minimal CMV promoter driving BFP expression and PGK promoter driving mCherry expression. Medium containing the viral particles was collected from Lenti-X 293T cells, filtered through a 0.45-µm filter and added to the immune cells for 24 h. Sorted cells were expanded in their respective medium and cryopreserved for further experiments.

In vitro stimulation of synNotch T cells through ICEp. SynNotch CD4$^+$ or CD8$^+$ primary T cells or murine cell lines (2.5×10^4) were cocultured with target cancer cells at a 1:1 ratio, with the addition of ICEp at 0.075 OD$_{550} \times 200$ µl of medium (100 µl of T-cell medium + 100 µl of cancer-cell medium) (unless otherwise specified). Dual-antigen-positive (GFP and HER2) target cells (A375 and K562) and GFP-positive K562 cells were used as positive controls. After mixing, cells

were centrifuged for 2 min at 300g to initiate interaction between the cells. After 24 h, the cocultures from CD8$^+$ T cells were stained with anti-CD69 antibody (BD, catalogue no. 562884), analysed by flow cytometry (BD LSR II) and imaged through the spinning disk confocal microscope (Nikon Yokogawa CSU-22). After 48 h, cytokine concentration in the supernatant was measured by IL-2 ELISA (for CD4$^+$ T cells, eBiosciences, catalogue no. BMS2221HS) and interferon-γ (IFN-γ) ELISA (for CD8$^+$ T cells, ThermoFisher, catalogue no. KHC4021).

To quantify target-cell killing, 2.5×10^4 A375 cells were seeded on a flat-bottomed 96-well tissue culture plate (Falcon, catalogue no. 353072) and cultured for 8 h, followed by the addition of 2.5×10^4 CD8$^+$ T cells and ICEp at 0.075 OD$_{550} \times 200$ µl final (unless otherwise specified). After 1–3 days, cells were gently washed with PBS twice and analysed for cell viability using PrestoBlue Cell Viability Reagent (Invitrogen, catalogue no. A13262).

Particle localization and retention assay through IVIS imaging and tumour section. A Cy3-labelled PLGA polymer (1 mg), as described above, was incorporated into the emulsion protocol for DNA-scaffolded (G or B strand) PLGA microparticles. The surface of the particles was then hybridized with a 5′-Quasar705 (Q705)-modified compG strand, 5′-IR800CW-modified compG strand or 5′-Q670-modified compB strand. Thereafter, human FITC-IgG (Sigma, catalogue no. SLBW7799) was loaded on the surface through step-by-step conjugation. NSG mice (Jackson Laboratory, catalogue no. 005557, female, ~8–12 weeks old) were implanted with xenograft tumours: 5×10^6 K562 tumour cells subcutaneously either at the right flank or on both flanks. All mice were maintained in pathogen-free, ventilated cages with irradiated food and autoclaved water in housing conditions of humidity at 30–70%, temperature at 20–26ºC and 12-h/12-h dark/light cycle at the Laboratory Animal Resource Center (LARC) facilities at UCSF. All mice used throughout the work were handled under local, state and federal guidelines following an Institutional Animal Care and Use Committee (IACUC)-approved protocol at UCSF. Mice were monitored daily and euthanized by CO$_2$ asphyxiation and cervical dislocation prior to any signs of distress.

For IVIS animal imaging, 100 OD$_{550} \times 50$ µl of particles with Q705-labelled DNA and FITC-IgG, or 1 nmol free IR800CW carboxylate dye (Li-COR, catalogue no. LIC-929-08972), were injected intratumorally 10 days after tumour implantation and imaged under the IVIS 100 preclinical imaging system (Xenogen, catalogue no. 124262, with PerkinElmer Living Image Software v.4.5.4) every 3-4 h for the first 48 h and every 8 h for the next 5 days. Images were analysed using PerkinElmer Living Image Software v.4.5.4.

For the tumour section analysis, 100 OD$_{550} \times 50$ µl of particles with Q670-labelled on DNA and FITC-IgG on surfaces, and Cy3 in the core, were injected intratumorally 10 days after tumour implantation. At 6 h, 2 days, 4 days and 6 days after particle injection, mice were euthanized and the tumour and several organs, including the heart, lung, liver, kidney and spleen, were collected. These tissues were imaged under the IVIS imaging system. Tumours were fixed in 4% paraformaldehyde (Electron Microscopy Sciences, catalogue no. 15710) overnight, then dehydrated in 30% sucrose (Sigma, catalogue no. S9378) for 1–2 days until the tumours sunk. Tumours were then snap-frozen in OCT (Tissue-Tek) to produce cryosections. Sections were imaged by the spinning disk confocal fluorescence microscope (Nikon Yokogawa CSU-22), and images were analysed using the MFI of the FITC and Q670 signals at particle locations identified by Cy3 signal using ImageJ v.2.0.0 software.

Safety tests of DNA-scaffolded nano-/microparticles. BALB/c mice (Jackson Laboratory, catalogue no. 000651, female, ~7–9 weeks old) were intravenously injected with PLGA nanoparticles (~250 nm diameter) and microparticles (~1.5 µm diameter) with DNA scaffolds and mouse isotype IgG2b (Bio X Cell, catalogue no. BP0086) tethered through hybridization-mediated assembly. The injection dose was 20 OD$_{550} \times 100$ µl for nanoparticles and 80 OD$_{550} \times 100$ µl for microparticles, with an equivalent amount of surface DNA (~1.3 nmol) and isotype IgG (~20 µg). Blood was collected 2 days after particle injection and centrifuged at 14,000g for 5 min to collect the serum. Serum samples (50 µl) diluted in 200 µl PBS were sent to San Francisco General Hospital Clinical Laboratory for clinical chemistry tests. Serum samples (50 µl) serum samples diluted in 50 µl of PBS were sent to Eve Technologies for cytokine/chemokine test (mouse cytokine/chemokine array 31-plex, MD31).

In vivo tumour targeting. NSG mice (Jackson Laboratory, catalogue no. 005557, female, ~8–12 weeks old) were implanted with two identical xenograft tumours: 5×10^6 HER2$^+$K562 tumour cells subcutaneously on the left and right flank. Seven days after tumour implantation, human primary CD4$^+$ (4×10^6) and CD8$^+$ T cells (4×10^6) were injected intravenously into the tail vein of the mice. These T cells were either untransduced (control) or engineered with the anti-GFP synNotch Gal4VP64 receptor and the corresponding response elements regulating anti-HER2 4-1BB CAR expression. On the same day, ICEp-GFP particles were injected intratumorally on one side of the two flanks with 50 (or 10) OD$_{550} \times 50$ µl per dose, leaving the other as the control. Three additional doses of ICEp were injected into the same tumour every 4 days or starting as soon as the tumour grew over 500 mm³ in volume. Tumour size was monitored via caliper over 20 days

after T-cell injection. Mice were euthanized when any tumour reached 20 mm in diameter or became ulcerated.

Remaining tumours from the contralateral flank and early euthanized mice were collected and fixed in 4% paraformaldehyde (Electron Microscopy Sciences, catalogue no. 15710) overnight, then dehydrated in 30% sucrose (Sigma, catalogue no. S9378) for 1–2 days until the tumours sunk. Tumours were then snap-frozen in OCT (Tissue-Tek) to produce cryosections. Sections were stained with anti-CD3 antibody (Biolegend, catalogue no. 344811) in 1% BSA/PBS for 1 h and washed three times, then imaged with the spinning disk confocal fluorescence microscope (Nikon Yokogawa CSU-22).

Statistical analysis. Statistical analyses were performed using GraphPad Prism v.8.4.3 software. All values and error bars are mean ± s.d., except where indicated differently. Two-tailed *t*-test, multiple *t*-test, one-way analysis of variance (ANOVA) test, two-way ANOVA test, linear regression, log-normal fit, nonlinear fit by the Michaelis–Menten model, Hill slope-specific binding model and fourth-order polynomial model fit were performed and specified where appropriate.

Reporting Summary. Further information on research design is available in the Nature Research Reporting Summary linked to this article.

Data availability
The original data of the gel electrophoresis images are publicly available at Dryad Digital Repository (https://doi.org/10.7272/Q6CC0XXJ). Any other raw data that support the plots within this paper are available from the authors upon reasonable request.

Author contributions
X.H., J.Z.W., R.C., K.T.R., W.A.L. and T.A.D. designed the experiments and interpreted the results. X.H., J.Z.W., R.C., Z.L., C.E.B., R.H.-L., I.S., E.G. and W.Y. performed the experiments, and D.M.P. contributed to material designs and synthesis. X.H. analysed the data and drafted the manuscript. X.H., J.Z.W., R.C., I.S., W.A.L. and T.A.D. edited the manuscript.

Competing interests
T.A.D., W.A.L., X.H., J.Z.W. and R.C. are inventors of pending patents related to the technology described in the manuscript. Z.L., C.E.B., R.H.-L., I.S., E.G., D.M.P., W.Y. and K.T.R. declare no competing interests.

Additional information
Supplementary information is available for this paper at https://doi.org/10.1038/s41565-020-00813-z.

Correspondence and requests for materials should be addressed to W.A.L. or T.A.D.

Peer review information *Nature Nanotechnology* thanks the anonymous reviewers for their contribution to the peer review of this work.

Reprints and permissions information is available at www.nature.com/reprints.

Corresponding author(s):	Tejal A. Desai Wendell A. Lim
Last updated by author(s):	10/14/2020

Reporting Summary

Nature Research wishes to improve the reproducibility of the work that we publish. This form provides structure for consistency and transparency in reporting. For further information on Nature Research policies, see <u>Authors & Referees</u> and the <u>Editorial Policy Checklist</u>.

Please do not complete any field with "not applicable" or n/a. Refer to the help text for what text to use if an item is not relevant to your study.
<u>For final submission</u>: please carefully check your responses for accuracy; you will not be able to make changes later.

Statistics

For all statistical analyses, confirm that the following items are present in the figure legend, table legend, main text, or Methods section.

n/a	Confirmed	
☐	☒	The exact sample size (n) for each experimental group/condition, given as a discrete number and unit of measurement
☐	☒	A statement on whether measurements were taken from distinct samples or whether the same sample was measured repeatedly
☐	☒	The statistical test(s) used AND whether they are one- or two-sided *Only common tests should be described solely by name; describe more complex techniques in the Methods section.*
☐	☒	A description of all covariates tested
☐	☒	A description of any assumptions or corrections, such as tests of normality and adjustment for multiple comparisons
☐	☒	A full description of the statistical parameters including central tendency (e.g. means) or other basic estimates (e.g. regression coefficient) AND variation (e.g. standard deviation) or associated estimates of uncertainty (e.g. confidence intervals)
☐	☒	For null hypothesis testing, the test statistic (e.g. F, t, r) with confidence intervals, effect sizes, degrees of freedom and P value noted *Give P values as exact values whenever suitable.*
☒	☐	For Bayesian analysis, information on the choice of priors and Markov chain Monte Carlo settings
☒	☐	For hierarchical and complex designs, identification of the appropriate level for tests and full reporting of outcomes
☒	☐	Estimates of effect sizes (e.g. Cohen's d, Pearson's r), indicating how they were calculated

Our web collection on <u>statistics for biologists</u> contains articles on many of the points above.

Software and code

Policy information about <u>availability of computer code</u>

Data collection	Tecan SparkControl Software V2.1 was used to collect data for fluorescence quantification on plates. NIS Elements AR 5.21.00_b1483 was used to acquire confocal fluorescent images. BD FACSDiva Software 8.0.1 was used to collected data from flow cytometer. PerkinElmer Living Image Software 4.5.4 was used to take mouse IVIS images.
Data analysis	GelQuantNET 1.8 was used for gel densitometry analysis. ImageJ 2.0.0 was used to quantify images of particles and cells. FlowJo 10.7.1 was used to analyze the flow cytometry data. PerkinElmer Living Image Software 4.5.4 was used to quantify mouse IVIS images. GraphPad Prism 8.4.3 was used to perform statistic analysis.

For manuscripts utilizing custom algorithms or software that are central to the research but not yet described in published literature, software must be made available to editors/reviewers. We strongly encourage code deposition in a community repository (e.g. GitHub). See the Nature Research <u>guidelines for submitting code & software</u> for further information.

Data

Policy information about <u>availability of data</u>

All manuscripts must include a <u>data availability statement</u>. This statement should provide the following information, where applicable:
- Accession codes, unique identifiers, or web links for publicly available datasets
- A list of figures that have associated raw data
- A description of any restrictions on data availability

The original data of the gel electrophoresis images are publicly available at Dryad Digital Repository (https://doi.org/10.7272/Q6CC0XXJ). Any other raw data that support the plots within this paper are available from the authors upon reasonable request.

Field-specific reporting

Please select the one below that is the best fit for your research. If you are not sure, read the appropriate sections before making your selection.

☒ Life sciences ☐ Behavioural & social sciences ☐ Ecological, evolutionary & environmental sciences

Life sciences study design

All studies must disclose on these points even when the disclosure is negative.

Sample size	No statistical methods were used to predetermine the sample size. Sample sizes for experiments were estimated based on previous experiences and reports with similar setups that showed significance, for example, references 32,33,41,50 for particle-related characterizations, reference 24,32 for natural T cell activation and phenotype characterizations, and reference 20, 41 for animal studies. Sample size for individual data sets were described in figure legends.
Data exclusions	For in vivo studies, the tumor was excluded from size measurement as become ulcerated according to the pre-established criterion. The mice with ulcerated tumor on either flank were euthanized according to the animal protocol.
Replication	A majority of experiments were conducted at least two times, and the number of experimental repeats for individual assays were specified in figure legend. All attempts at replication were successful.
Randomization	Particles of the same feature used within a specific analysis were randomly assigned to different biomolecule coating conditions. Cells used for test experiments were randomly assigned to experimental groups with different treatments. Animals in tumor studies were randomized to groups equalizing mean tumor size at start of the treatment. No other randomization was performed.
Blinding	Experimenters was blinded to the group allocation during the tumor size measurement and during fluorescence image quantifications. No other blinding was performed.

Reporting for specific materials, systems and methods

We require information from authors about some types of materials, experimental systems and methods used in many studies. Here, indicate whether each material, system or method listed is relevant to your study. If you are not sure if a list item applies to your research, read the appropriate section before selecting a response.

Materials & experimental systems

n/a	Involved in the study
☐	☒ Antibodies
☐	☒ Eukaryotic cell lines
☒	☐ Palaeontology
☐	☒ Animals and other organisms
☒	☐ Human research participants
☒	☐ Clinical data

Methods

n/a	Involved in the study
☒	☐ ChIP-seq
☐	☒ Flow cytometry
☒	☐ MRI-based neuroimaging

Antibodies

| Antibodies used | For the quantification of surface loading of IgG on ICEp, human FITC-IgG from Sigma Cat#F9636 was used. For antibody activity validation post surface assembly, mouse anti-human PD-L1 (clone BE0285, BioXCell Cat#BE0285) and mouse PE anti-human PD-L1 (clone 29E.2A3, Biolegend Cat#329705) were used.

For the functionalization of ICEp for in vivo safety test, mouse isotype IgG2b (clone MPC-11, BioXcell Cat#BP0086) was used.

For the loading on ICEp particles for cell activation, following antibodies were used: mouse anti-human CD3 (clone OKT-3, BioXCell Cat#BE0001-2), mouse anti-human CD28 (clone 9.3, BioXCell Cat#BE0248), mouse anti-human IL-2 (clone 5355, ThermoFisher Cat#MA523696).

For flow cytometry analysis of T cell phenotype, following antibodies were used: mouse anti-human CCR7 (clone 150503, BD Cat#561271), mouse anti-human CD45RA (clone HI100, BD Cat#562885), mouse anti-human LAG-3 (clone T47-530, BD Cat#565720), mouse anti-human TIM-3 (clone 7D3, BD Cat#565559), mouse anti-human PD-1 (clone EH12.2H7, Biolegend Cat#329936), mouse anti-human CD69 (clone FN50, BD Cat#562883), mouse anti-human CCR7 (clone G043H7, Biolegend Cat#353226), mouse anti-human CD45RA (clone G043H7, Biolegend Cat#304150), mouse anti-human CD45RO (clone UCHL1, BD Cat#564291), mouse anti-human CD62L (clone DREG-56, Biolegend #304830), mouse anti-human CD27 (clone M-T271, Biolegend #356424), mouse anti-human CD95 (clone DX2, Biolegend #305644). |
|---|---|

Validation	FITC-IgG (Sigma) is quality controlled by the vendor and is cited by 6 peer reviewed papers (https://www.sigmaaldrich.com/catalog/product/sigma/f9636?lang=en&region=US)

FITC-IgG (Sigma) is quality controlled by the vendor and is cited by 6 peer reviewed papers (https://www.sigmaaldrich.com/catalog/product/sigma/f9636?lang=en&region=US)

anti-human PD-L1 (BioXCell) is validated by the vendor and is cited by 5 peer reviewed papers (https://bxcell.com/product/invivomab-anti-human-pd-l1-b7-h1/)

anti-human PD-L1 (Biolegend) is validated by the vendor and is cited by 26 peer reviewed papers (https://www.biolegend.com/en-us/products/pe-anti-human-cd274-b7-h1--pd-l1-antibody-4375)

mouse isotype IgG (BioXCell) is validated by the vendor and is cited by 5 peer reviewed papers (https://bxcell.com/product/invivoplus-mouse-igg2b-isotype-control-unknown-specificity/)

anti-human CD3 (BioXCell) is validated by the vendor and is cited by 8 peer reviewed papers (https://bxcell.com/product/h-cd3/)

anti-human CD28 (BioXCell) is validated by the vendor and is cited by 3 peer reviewed papers (https://bxcell.com/product/h-cd28/)

anti-human IL-2 (ThermoFisher) is validated by the vendor (https://www.thermofisher.com/antibody/product/IL-2-Antibody-clone-5355-Monoclonal/MA5-23696)

anti-human PD-L1 (BioXCell), anti-CD3 (BioXCell), anti-CD28 (BioXCell) that were conjugated with complementary DNA using our protocol were validated using PD-L1 over-expressing K562 cells (for anti-PD-L1) and human primary T cells (for anti-CD3 and anti-CD28). anti-IL-2 (ThermoFisher) was engineered on ICEp, validated and quantified through IL-2 binding assay (EILISA, Supplementary Fig. 6j)

anti-human CCR7 (BD) is validated by the vendor and is cited by 10 peer reviewed papers (https://www.bdbiosciences.com/eu/applications/research/t-cell-immunology/th-2-cells/surface-markers/human/fitc-mouse-anti-human-cd197-ccr7-150503/p/561271)

anti-human CD45RA (BD) is validated by the vendor and is cited by 3 peer reviewed papers (https://www.bdbiosciences.com/eu/applications/research/t-cell-immunology/regulatory-t-cells/surface-markers/human/bv421-mouse-anti-human-cd45ra-hi100/p/562885)

anti-human LAG-3 (BD) is validated by the vendor and is cited by 5 peer reviewed papers (https://www.bdbiosciences.com/eu/reagents/research/antibodies-buffers/immunology-reagents/anti-human-antibodies/cell-surface-antigens/bv421-mouse-anti-human-lag-3-cd223-t47-530/p/565720)

anti-human TIM-3 (BD) is validated by the vendor and is cited by 12 peer reviewed papers (https://www.bdbiosciences.com/eu/reagents/research/antibodies-buffers/immunology-reagents/anti-human-antibodies/cell-surface-antigens/alexa-fluor-647-mouse-anti-human-tim-3-cd366-7d3/p/565559)

anti-human PD-1 (Biolegend) is validated by the vendor and is cited by 4 peer reviewed papers (https://www.biolegend.com/en-us/products/alexa-fluor-488-anti-human-cd279-pd-1-antibody-9863)

anti-human CD69 (BD) is validated by the vendor and is cited by 3 peer reviewed papers (https://www.bdbiosciences.com/eu/applications/research/b-cell-research/surface-markers/human/bv421-mouse-anti-human-cd69-fn50-also-known-as-fn-50/p/562883)

anti-human CCR7 (Biolegend) is validated by the vendor and is cited by 22 peer reviewed papers (https://www.biolegend.com/en-us/products/pecyanine7-anti-human-cd197-ccr7-antibody-7694)

anti-human CD45RA (Biolegend) is validated by the vendor and is cited by 16 peer reviewed papers (https://www.biolegend.com/en-us/products/apc-anti-human-cd45ra-antibody-684)

anti-human CD45RO (Biolegend) is validated by the vendor and is cited by 5 peer reviewed papers (https://www.bdbiosciences.com/eu/reagents/research/antibodies-buffers/immunology-reagents/anti-human-antibodies/cell-surface-antigens/buv395-mouse-anti-human-cd45ro-uchl1/p/564291)

anti-human CD62L (Biolegend) is validated by the vendor (https://www.biolegend.com/en-gb/products/brilliant-violet-785-anti-human-cd62l-antibody-7974)

anti-human CD27 (Biolegend) is validated by the vendor (https://www.biolegend.com/en-gb/products/apc-cyanine7-anti-human-cd27-antibody-12841)

anti-human CD95 (Biolegend) is validated by the vendor (https://www.biolegend.com/en-gb/products/brilliant-violet-711-anti-human-cd95-fas-antibody-13543)

Eukaryotic cell lines

Policy information about cell lines

Cell line source(s)	K562 and A375 cell lines were sourced from the ATCC, and BA/F3, DSMZ and 32D were sourced from DSMZ.
Authentication	The cell lines used have not been further authenticated.
Mycoplasma contamination	All cell lines tested negative for mycoplasma contamination.
Commonly misidentified lines (See ICLAC register)	No commonly misidentified cell lines were used.

Animals and other organisms

Policy information about studies involving animals; ARRIVE guidelines recommended for reporting animal research

Laboratory animals	Female NSG mice (NOD.Cg-Prkdc-scid IL2rg-tm1Wjl/SzJ, #005557) 6-8 weeks of age, and female BALB/c mice (#000651) 7-9 weeks of age were purchased from Jackson Laboratories (Bar Harbor, Maine, USA). NSG mice were implanted with xenograft tumors at 8-12 weeks of age. All mice were maintained in pathogen-free, ventilated cages with irradiated food and autoclaved water in housing conditions of humidity at 30-70%, temperature at 20-26 C and 12/12 dark/light cycle at the Laboratory Animal Resource Center (LARC) facilities at University of California San Francisco (UCSF). Mice were monitored daily and euthanized by CO_2 asphyxiation and cervical dislocation prior to any signs of distress.

Wild animals	No wild animal was used.
Field-collected samples	No field-collected samples were used.
Ethics oversight	All mice used throughout the work were handled under local, state and federal guidelines following an Institutional Animal Care and Use Committee (IACUC)-approved protocol at UCSF.

Note that full information on the approval of the study protocol must also be provided in the manuscript.

Flow Cytometry

Plots

Confirm that:

☒ The axis labels state the marker and fluorochrome used (e.g. CD4-FITC).

☒ The axis scales are clearly visible. Include numbers along axes only for bottom left plot of group (a 'group' is an analysis of identical markers).

☒ All plots are contour plots with outliers or pseudocolor plots.

☒ A numerical value for number of cells or percentage (with statistics) is provided.

Methodology

Sample preparation	All antibody staining for flow cytometry was carried out in wells of round bottom 96-well tissue culture plates. Cells were pelleted by centrifugation of plates for 4 minutes at 400 x g. Supernatant was removed and cells were resuspended in 50 μL PBS containing the fluorescent antibody of interest. Cells were stained for 25 minutes at 4°C in the dark. Stained cells were then washed twice with PBS and resuspended in fresh PBS for flow cytometry.
Instrument	BD LSR II, BD LSRFortessa and BD FACSAria II
Software	Collection: BD FACSDiva Software 8.0.1; Analysis: FlowJo 10.7.1
Cell population abundance	For analysis, at least 20,000 cells gated from forward and side-scatter characteristics were acquired for all FACS analysis.
Gating strategy	All cells were gated based on forward and side-scatter characteristics to limit debris including dead cells and particles. Gating of "Positive" and "negative" biomarker staining were specified in figures and supplementary figures.

☒ Tick this box to confirm that a figure exemplifying the gating strategy is provided in the Supplementary Information.